Supporting Information for

Relationship between rupture length and magnitude of oceanic transform fault earthquakes

Guilherme de Melo[1], Ingo Grevemeyer[1], Dietrich Lange[1], Dirk Metz[2], and Heidrun Kopp[1]

[1] GEOMAR Helmholtz Centre of Ocean Research Kiel, Kiel, Germany.

[2] Preparatory Commission for the Nuclear-Test-Ban Treaty Organization (CTBTO), Vienna, Austria.

Contents of this file

In this document, we provide material supporting the manuscript. We include four sections with 15 figures and four tables. Table S1 lists the rupture parameters obtained with T-waves of all 47 earthquakes. Text S1 reviews previous studies applying our technique and provides details on assessing T-wave azimuth and epicenter determinations (Figure S1-S9). Figure S09 and Table S02 compare our average back-azimuth obtained with T-wave and the epicenters of different global catalogs. We compared the new epicenters obtained from the average back-azimuth with the relative relocated epicenters obtained from the teleseismic waveform model method of McGuire (2008). Details about the comparison with relative location are described in Figure S10a and Table S2. Lastly, we include details about the uncertainties of the rupture lengths measured (Figure S10b; Table S1).

Text S2 provides additional details on the results, comparing our rupture lengths with the Global Centroid Moment Tensor (GCMT, Ekström et al., 2012) moment magnitudes and epicentral distances. Further, we discuss the hydroacoustic energy generated by earthquakes, called source level (SL). The dependency of SL on earthquake properties is shown in Figure S11 and listed in Table S4. Moreover, we summarize the main features of each of the 11 transforms. In addition, we show a strong correlation between our rupture lengths and the approximated rupture durations from the SCARDEC source time functions (Vallée and Doute, 2016; Figure S12). Figure S13 compares the total T wave duration with rupture lengths, magnitudes, and source time functions for earthquakes from the SCARDEC catalog (http://scardec.projects.sismo.ipgp.fr/).

Text S3 compares our rupture lengths obtained from T-waves with the lengths from the finite fault models by the USGS (Figures S14-S15).

Text S4 provides additional details on the relationship between Mw and parameters controlling earthquake length.

Text S1: *Hydroacoustic versus seismological estimation of rupture for submarine earthquakes*

The technique used in our study was previously used to study subduction zone megathrust earthquakes, and here we summarize the constraints of these studies. For our brief introduction, we chose an earthquake where a wealth of seismological studies has investigated the same earthquake, i.e., the great Sumatra earthquake of 2004. Three studies applied similar techniques to derive robust back-azimuth estimates from T-waves and reveal details of the rupture behavior, including changes in the velocity of rupture propagation (de Groot-Hedlin, 2005; Guilbert, et al., 2005; Tolstoy and Bohnenstiehl, 2005) and the length of a 1200-1235 long rupture zone (Guilbert et al., 2005; Tolstoy and Bohnenstiehl, 2005). Guilbert et al. (2005) used both hydroacoustic and seismic array data and found matching results on both rupture propagation and the size of the rupture zone. Shearer and Bürckmann (2010) found for the giant 2004 Sumatra earthquake that rupture length estimates from the hydroacoustic studies agree well with results from seismological and geodetic data, suggesting that T-waves carried important information on the properties of seismic faulting.

Additional information on data processing

Our technique is based on back-azimuth estimations, as described in the methodology section of the paper. Figures S01-S04 show the unfitted results of the 2023 Mw 5.6 St. Paul-A and 2017 Mw 6.6 Chain earthquake, providing data from each hydrophone channel and illustrating the resulting output of the processing, i.e., measured delay, calculated back-azimuth and rupture velocity.

Figures S05-S08 show for the Mw=7.1 2016 Romanche and Mw=6.5 2020 St. Paul earthquake, the processing output (back-azimuth, closure, and cumulative rupture and corresponding rupture length; RL) as well as the back-projection in map view. The complete catalog can be found on Zenodo (https://doi.org/10.5281/zenodo.12580246).

Accuracy and benchmarking

Transform fault earthquakes generally rupture the seafloor at water depths deeper than the waveguide of the SOFAR channel. We, therefore, explore the accuracy of T-wave derived back-azimuths by comparing the average back-azimuth to epicenter locations from global catalogs. We hypothesized that the epicenter, or location of the seismic-to-acoustic conversion point (Okal, 2008), would be at the average back-azimuth. This implies that the T-wave source location may not correspond precisely to the epicenter location reported by global catalogs at teleseismic distances (Talandier and Okal, 1998). We took two approaches: 1) We determined the difference between the T-wave back-azimuth and the back-azimuth directed to the epicenter reported by global catalogs, and 2) we compared the distance between 15 pairs

of T-wave epicenters to the relative epicenters derived from cross-correlating surface waves for the same respective earthquakes (McGuire, 2008).

Comparison with the epicenters of global catalogs

We compared the locations of our new T-wave epicenter locations with the epicenter coordinates reported by GCMT (Ekström et al., 2012), IPGP (Romanowicz et al., 1984; Vallée and Doute, 2016), and USGS (U.S. Geological Survey, 2024) global catalogs. We compared the distance between the epicenters and back-azimuth difference for all 47 earthquakes. The back-azimuth is calculated by comparing the back-azimuth of the T-wave with the back-azimuth of the epicenter location reported global networks in relation to the H10N array.

Compared to the GCMT location, the T-wave epicenters deviate by 2.2 to 32.5 km with an average of 15.5±8.2 km (Figure S09). We identified a back-azimuth discrepancy with an average of 0.65º. The distances between T-wave and IPGP epicenters vary between 1.24 and 47 km with an average of 15.8±11 km and an average difference of the back-azimuth of 0.48º. With respect to the USGS epicenter, the azimuths deviate by 0.42°. The distances between our and USGS epicenter locations vary from 1.24 to 49.82 km with an average of 16.2±12.4 km. One of the main reasons for this discrepancy is that most epicenters of the global catalogs are located away from the transform valley, and it was shown that global earthquakes might be shifted by several tens of kilometers from the actual source (e.g., Pan et al., 2002; Grevemeyer et al., 2013). Despite that, Pan and Dziewonski (2005) observed that the relocated GCMT epicenters of the Atlantic Ocean show locations closer to hydroacoustic locations than the global ISC (International Seismic Centre, www.isc.ac.uk) catalog. Table S2 lists the hypocentral locations of earthquakes for the different catalogs.

Relative relocation using teleseismic record

To compare the epicenter from our hydroacoustic locations with global seismic observations, we used surface waves and cross-correlation to relocate the GCMT centroid locations of earthquake pairs and assess the distance between two earthquakes of similar focal mechanisms. We compare the distance between them with the distance of the same pair of events derived from T-waves. We assume that a T-wave epicenter occurs where the mean azimuth of the T-wave ray path crosses the trace of the transform fault derived from multibeam bathymetric data. To calculate the new relative epicenters from surface waves, we follow the procedure described in McGuire (2008). The algorithm uses the differential travel time between the two-peak cross-correlation signals to obtain the new relative position. The surface wave records are bandpass filtered between 0.02-0.04 Hz. The methodology assumes that the two paired earthquakes have equal focal mechanisms (McGuire, 2008). We analyzed only those earthquakes

contained in our T-wave rupture catalog and found a total of 30 earthquakes and 15 pairs (Table S3). The synthetic and observed waveforms of all 15 pairs are shown in figures on Zenodo (https://doi.org/10.5281/zenodo.12580246), together with other figures showing maps with the master and relocated epicenters obtained by teleseismic surface waves and the epicenters obtained using the T-wave. The distances between the master and relocated epicenter vary from 1.9 to 37 km, with a mean of 14.7 km. The epicenters located using the T-waves of the same pairs show a mean of 11.5 km, and the distances between them have a range of 1.1-34.6 km. Figure S10 shows a comparison of the distance between the relatively relocated epicenter pairs and the distance between pairs of T-wave epicenters.

Please note that our method is not limited to earthquakes but is valid for any hydroacoustic form of energy arriving at the hydrophone array. For example, Metz et al. (2021) located a sinking cargo ship using T-wave energy recorded at a distance of 7,330 km, locating its position with an accuracy within 0.1°.

Uncertainties of rupture lengths

The BAZ obtained from the array analysis changes systematically for each earthquake, suggesting systematic rupture propagation. To assess the smallest angular change we can resolve, we studied the distribution of relative BAZ changes or back-azimuth differences (BAZD). The errors of the rupture lengths and rupture velocities were assessed to reveal uncertainties and avoid interpreting poorly constrained lengths. We estimated the error for the RLs in three steps: 1) cross-correlation of all time windows of the wavetrain to obtain the back-azimuth; 2) calculation of BAZD between the nth and the n+1 cross-correlated time-window, providing an approximation of the smallest relative change of BAZ we can resolve. Independent of magnitude, the largest number of BAZD occurs at approx. 0.1° (Figure S10b); unfortunately, we have no independent means to calibrate BAZD using any master events and therefore assume for simplicity that any BAZD $\geq$0.1° is well resolved. Interestingly, the largest BAZD values of >1.0° (1.09°, 1.40°, 1.50°) all refer to supershear steps in the rupture process of the 2016 Mw 7.1 and 2022 Mw 6.9 Romanche earthquakes. Last, 3) we calculated the estimated rupture length error (RLE) from the epicentral distance (Δ) and the smallest resolved BAZ, i.e., RLE=tan (0.1°)*Δ.

Any uncertainty in the back-azimuth will cause an error in assessing the rupture length, which, in turn, will increase with increasing epicentral distances. The smallest uncertainty is estimated to be just ±0.36 km for the 2020 Mw 5.6 Ascension earthquake. The largest uncertainty of ±6.62 km occurs for the most distance events at the Vema OTF. Compared to the magnitude and rupture lengths, we identified that the earthquakes with Mw<6.0 have a higher range of relative uncertainty ranging from 2.9% to 57% of their RL (Table S1), while the earthquakes Mw=>6.0 present a smaller RLE from 2 to 12% compared to their RL. Please note that for events with a significant relative rupture length error, the rupture velocity is marked to be unreliable (see rupture velocity marked with asterisks in Table S1).

Text S2: *Moment magnitude and source level relation*

The seismic source region and the source area obtained by hydroacoustic data can vary because T-wave energy is affected not only by the ground motion of the seabed but also by multi-pathing along the hydroacoustic travel path (Talandier and Okal, 1998). Especially local seafloor morphology in the vicinity of the rupture (e.g., seamounts, ridges, or other seafloor features) may radiate energy into the water column, which can be altered during its propagation in the SOFAR channel (Dziak 2001).

We compare the GCMT moment magnitudes of the 47 earthquakes with the acoustic energy that the earthquake released into the water column and received by the hydrophone array (Table S4). The underwater energy is defined as the source level (SL), also called acoustic magnitude (Bohnenstiehl et al., 2003), calculated by

$$SL = RCL + TL$$

RCL is the receiver level recorded by the hydrophone, and TL is the transmission loss attenuated over underwater propagation (Erbe, 2011). TL can be calculated by

$$TL = 20 \log_{10}(H/1m) + 10 \log_{10}(R/H) = 10 \log_{10}(H/1m) + 10 \log_{10}(R/1m)$$

where R is the horizontal distance from the source to the receiver location, H refers to the water depth of the source, and 1 m is the reference distance (Dziak 2001; Erbe 2011). We estimated H using the position of the epicenter coordinates and the global bathymetric data model SRTM15 (Tozer et al., 2019). We obtained a regression of the epicentral distance versus the SL with a correlation coefficient of 0.54 (Figure S11a). Also, we obtained coefficients of 0.52 and 0.54 comparing Mw and rupture length versus SL (Figures S11b, c). The results confirm that the hydroacoustic signatures provide a good correlation with both Mw and the rupture parameters.

Estimates of rupture lengths and rupture direction: transform-by-transform

The Ascension transform (~7°S) is located nearest the hydrophone triplet at about 100 km to the northeast, providing two earthquakes of Mw 5.6 and 5.9 with RLs ranging from 8.2-13.8 km. At the Chain (1°S), four Mw 5.6-6.3 earthquakes occurred and produced cumulative ruptures ranging from 4.5±0.3 km to 38.7±1.9 km. The Romanche transform (1.2°S-0.2°N) at the equator provided 21 earthquakes with Mw 5.6-7.1 ranging in length from 6.3±0.6 km to 102.6±7.2 km (note: rupture length was shorter:81 km). The largest event, the 2016 Mw 7.1 earthquake, was one of the few events showing a more complex rupture

pattern, reversing its rupture direction over time. In the St. Paul transform system (St.Paul A, B, C; 0.6-1.0°N), nine earthquakes of Mw 5.6-6.9 occurred with ruptures ranging from 7.9±2.2 km to 65.6±3 km in length, with the longest rupture occurring in the St. Paul-B (0.85°N) segment located ~1780 km away of the array. The Bogdanov transform (7.2°N, ~2760 km distance) revealed a single Mw 5.7 earthquake with a rupture of 11.4±1.4 km. The Pushcharovsky (7.4°N) earthquake had an RL of 43.4±2.2 km and Mw 6.5. The hydroacoustic signature along the Vernadsky (7.7°N) revealed ruptures ranging from 6.6±2.2 to 50.3±3.0 km in four earthquakes (Mw 5.6-6.6). Two earthquakes of magnitudes 6.5 and 6.6 hit the Doldrums transform (8.2°N), showing rupture extents of 46.1±6.1 km and 63.3±3.5 km. Three earthquakes occurred in the Vema transform (10.9°N), the most distant transform (~3803 km away). The magnitudes of Vema earthquakes range from 5.9 to 6.9, with the RLs ranging from 20.6±3.0 km to 73±5.9 km, with a single earthquake showing a two-step rupture.

Our estimates also reveal systematic changes in the back-azimuth, which reflects the direction of the rupture. Most events showed unilateral rupture or a domination of one direction, with 20 of the studied events rupturing eastward and 23 westward and only four events showing a change in rupture direction (see also discussion of the 2016 Mw=7.1 Romanche earthquake in the main text). Although there seemed to be a small preference for westward rupture, we tend to believe that the mismatch is related to a too small number of studied earthquakes. The rupture direction itself does not show any correlation with the age-offset of the transform fault. For example, at the Romanche and hence the transform with the largest age-offset, we observe ten versus nine events rupturing westwards or eastwards, respectively. In addition, we observe both eastward and westward rupture at either end of the Romanche transform. Interestingly, at the Chain, we observe a preference of eastward rupture (four out of five earthquakes and the fifth one showing a change of rupture direction over time).

In the equatorial Atlantic, increasing age-offset is mimicking the length of the fault zone and all events with Mw>6.2 occur in the longer offset faults (see also main text). However, the largest earthquakes do not necessarily occur in the middle of the faults. Thus, the 2016 Mw=7.1 Romanche earthquake ruptured near the eastern end of the Romanche and is among the largest observed earthquakes occurring in any transform fault. Nevertheless, we do not observe any Mw>5.9 earthquakes in the direct vicinity to any ridge-transform intersection.

Text S3: *Comparison with finite fault models from the USGS*

The United States Geological Survey (USGS) uses the finite fault inversion to model the quantity of fault slip for strong earthquakes (Ji et al., 2002). The methodology uses input parameters as GCMT solution (Ekström et al., 2012) and a Coulomb stress model (Toda et al., 2011). The length and width of the fault and the slip vary according to the earthquake magnitudes. The USGS analyzed the finite fault of the Mw 7.1 2016 and Mw 6.9 2022 Romanche earthquakes (Figures S14-S15). A cross-section of the slip distributions for the two earthquakes is shown in Figures S8-S9. For the Mw 7.1 2016 earthquake, the slip distribution along strike shows that the rupture extended for 75-95 km length. The slip distribution along the strike of the Mw 6.9 2022 shows the earthquake ruptured by a 65-85 km length. The rupture lengths of the two earthquakes obtained using the T-wave were 102.5±7.2 and 89.1±7.7 km, respectively.

Text S4*: Seismic moment and rigidity*

Kanamori (1977) defined that the energy released by earthquakes can be calculated by the moment magnitude (Mw), such as

$$Mw = \frac{2}{3} log_{10}(M_0) - 10.7$$

being that the seismic moment (M_0) can be obtained by the modulus of rigidity (μ), fault displacement (D), and the ruptured faulting area (A) calculated using the length (L) and width (f),

$$M_0 = \mu DA = \mu DfL$$

Then,

$$Mw = \frac{2}{3} log_{10}(\mu DfL) - 10.7$$

$$Mw = \frac{2}{3} log_{10}((\mu Df) + log_{10}(L)) - 10.7$$

$$Mw = \frac{2}{3} log_{10}(\mu Df) + 10^L - 10.7$$

$$\frac{Mw}{\frac{2}{3} log_{10}(Df\mu)} + 10.7 = 10^L$$

$$L = log_{10}\left(\frac{Mw}{\frac{2}{3} log_{10}(Df\mu)} + 10.7 \right)$$

Let us consider two different strike-slip earthquakes with the same magnitude Mw; one occurring in the continental lithosphere and the other in the oceanic lithosphere. In case both events have the same slip D and the same width f for both faults, the rupture lengths will depend only on the modulus of rigidity (μ).

Therefore, once the μ of the continental lithosphere is higher than μ of the oceanic lithosphere, the rupture length of the oceanic strike-slip earthquake should be longer than the rupture generated by the earthquake that occurred in the continental lithosphere.

To test the hypothesis, we calculated values of μ for rocks such as granite and diabase which are rocks common in continental crust, and serpentinized peridotite which refer to rocks commonly found on the seafloor of the oceanic transform faults (Searle, 2013). We know that μ can be calculated from the formula of S-wave velocity (Vs) and density of the rock (ρ),

$$V_S = \sqrt{\frac{\mu}{\rho}} = \frac{\sqrt{\mu}}{\sqrt{\rho}}$$

$$\sqrt{\mu} = V_S\sqrt{\rho}$$

$$\mu = V_S{}^2\rho$$

In most marine studies, Vs is not measured directly, but can be approximated from the P-wave velocity (Vp) and the ratio between P-wave and S-wave velocities (Vp/Vs). The Vp/Vs ratios are frequently used to study the lithological characteristics of the crust and mantle in both oceanic and continental settings (Buehler and Shearer, 2014; Grevemeyer et al., 2018; Liu et al., 2023). Grevemeyer et al. (2018) found that the Vp/Vs ratio in the oceanic crust is generally in the order of 1.8, while serpentinized mantle reaches values varying from 1.9 to 2.1. Experimental relationships between the volume of the serpentine rock (Φ) and Vp/Vs and Vp at 600MPa pressure (Ji et al., 2013; Li et al., 2024) reveal:

$$V_P = 8.10 - 3.00\Phi$$

$$\frac{V_P}{V_S} = 1.77 + 0.38\Phi$$

In the Atlantic Ocean, serpentinized peridotite dredged from transform faults shows a varying but generally high serpentine content. At the St. Paul, 30-60% (Φ=0.30-0.60) of the peridotites are hydrated (Hekinian et al., 2000; Campos et al., 2003; Bickert et al., 2023) and densities range from 2.30 to 3.31 kg/m^3 (Campos et al., 2003; Campos et al., 2022); at the Romanche about 80% of the mantle rocks are serpentinized ($\Phi = 0.80$) and density is in the order of 2.500 kg/m^3 (Gregory et al., 2021); at the Atlantis transform, peridotite rocks show the volume of serpentine ranging from 70 to 95% ($\Phi = 0.7 - 0.95$) and density of 2.8 to 3.200 kg/m^3 (Blackman et al., 2002). Thus, the modulus of the rigidity for the oceanic transform faults dominated by serpentinized peridotite can be obtained by

$$V_S = \frac{V_P}{1.77 + 0.38\Phi}$$

$$V_S = \frac{8.10 - 3.00\Phi}{1.77 + 0.38\Phi}$$

$$\mu = \left(\frac{8.10 - 3.00\Phi}{1.77 + 0.38\Phi}\right)^2 \rho$$

For the St. Paul transform, we approximate Vp=6.3 km/s, Vs=3.15 km/s, and Vp/Vs=1.99; at the Romanche transform we use Vp=5.7 km/s, Vs=2.74 km/s, and Vp/Vs=2.07; at the Atlantis we use Vp=5.25 km/s, Vs=2.46 km/s, and Vp/Vs=2.13. The values for the rigidity at the St. Paul, Romanche and Atlantis are in the order of $\mu = 0.24x10^{11}Pa$, $\mu = 0.19x10^{11}Pa$, and $\mu = 0.17x10^{11}Pa$, respectively.

For the continents, we calculated the modulus of rigidities for granite, diorite and diabase using properties measured by Christensen (1996) at 600MPa). Approximating Vs from both Vp and the Vp/Vs ratio rigidity and be calculated from:

$$\mu = \frac{V_P{}^2 \rho}{(V_P/V_S)^2}$$

For granite, ρ=2.652 kg/m^3, Vp=6.327 km/s, and Vp/Vs=1.707; for diorite ρ=2.936 kg/m^3, Vp=6.782 km/s, and Vp/Vs=1.771; for diabase ρ=2.810 kg/m^3, Vp=6.611 km/s nd Vp/Vs=1.805. Hence, rigidity can be approximated for granite, diorite and diabase with $\mu = 0.36x10^{11}Pa$, $\mu = 0.39x10^{11}Pa$, and $\mu = 0.41x10^{11}Pa$, respectively.

In general, the rigidity of oceanic transform faults characterized by serpentinized peridotites are 20 to 50% lower than for continental lithosphere, supporting our hypothesis of longer rupture lengths in oceanic transform faults for a given magnitude.
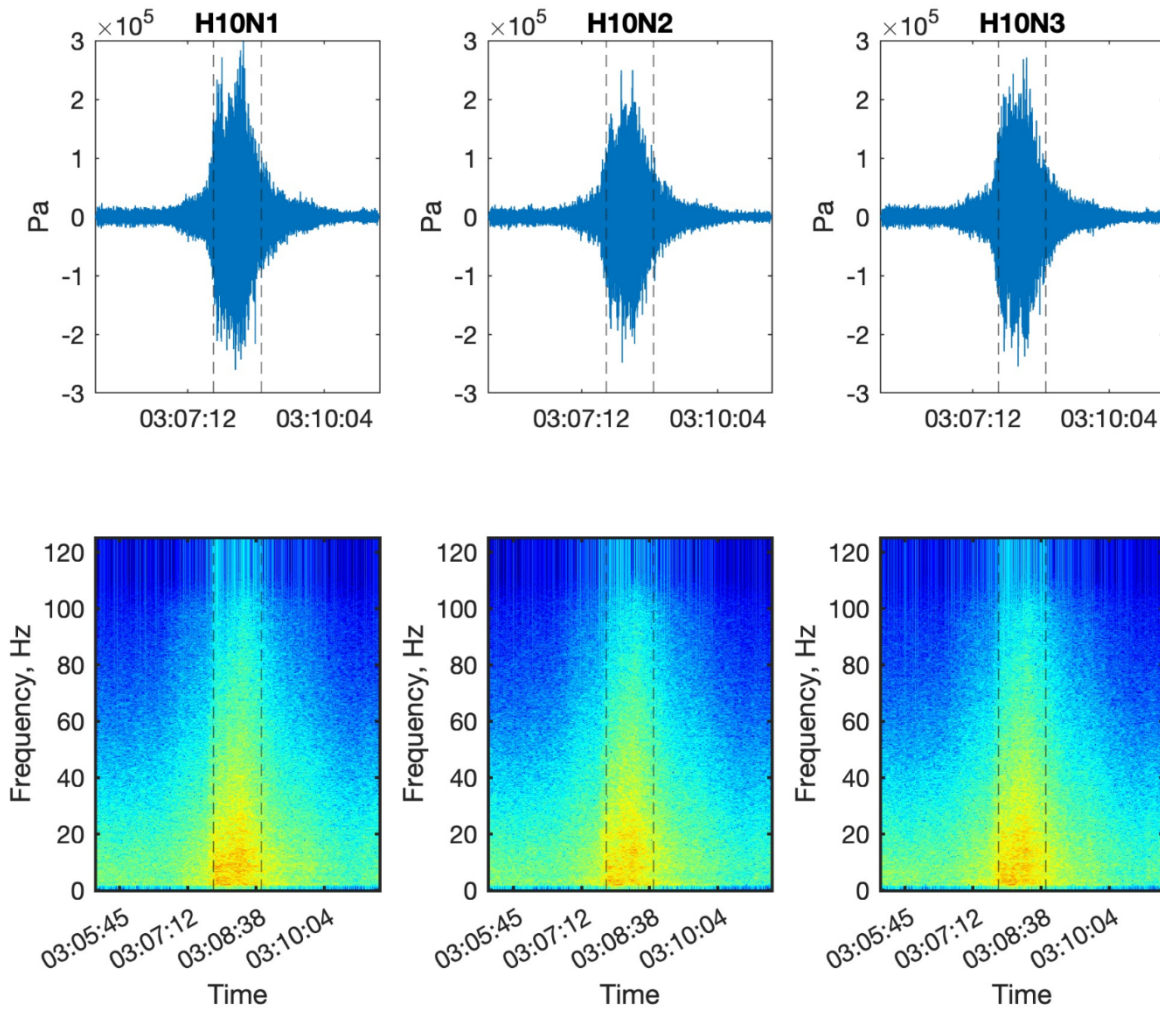
Figure S01. T-waveform and spectrogram of the Mw 6.6 Chain earthquake occurred on the 2017/08/18 at 02:59:39 and recorded by the three hydrophones (H10N1, H10N2, H10N3). A high pass filter of 2 Hz was applied to the signal. Vertical dotted lines show the earthquake window used for the azimuth estimates, identified from the high-frequency content.
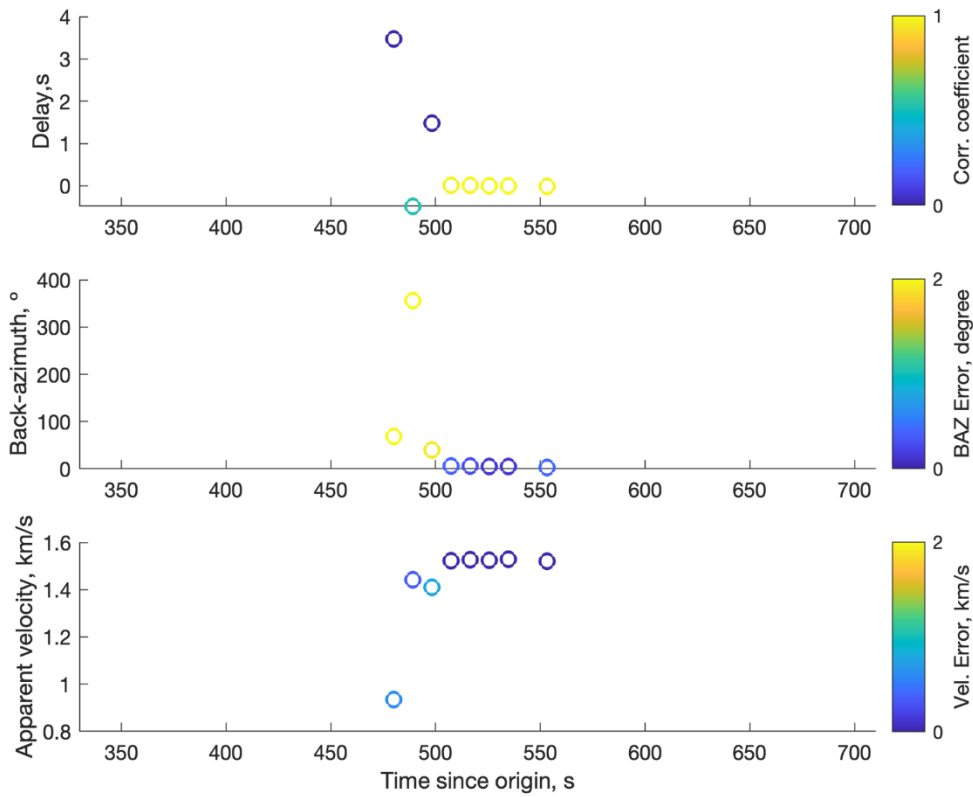
Figure S02. Results of the Mw 6.6 Chain earthquake from 2017/08/18 at 02:59:39. Upper panel: Summed time delays obtained from lag times in cross-correlation and mean correlation coefficient between hydrophone pairs. Middle panel: Back-azimuths averaged from the three-hydrophone pair cross-correlated, with all the time windows showing the same back-azimuth. Bottom: The apparent sound velocity is calculated as the mean across the array. The results show a low correlation coefficient with a high error in back-azimuth and apparent velocity at the beginning of the high-frequency waveform range.
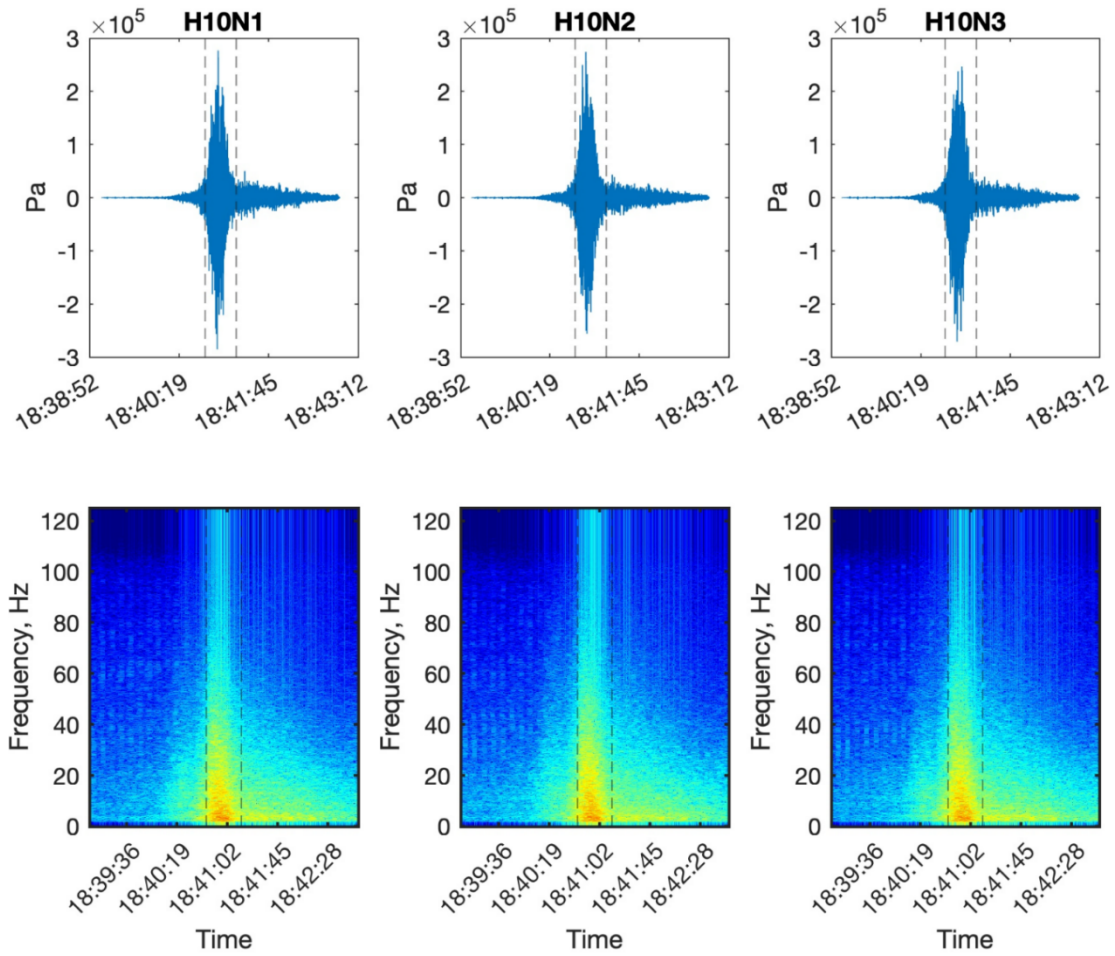
Figure S03. T-waves and spectrograms of the Mw 5.6 St. Paul earthquake occurred on 2023/01/03 at 18:19:29 and recorded by the three hydrophones (H10N1, H10N2, H10N3). A high pass filter of 2 Hz was applied to the signal. Vertical dotted lines show the earthquake window used for the azimuth estimates, identified from the high-frequency content.
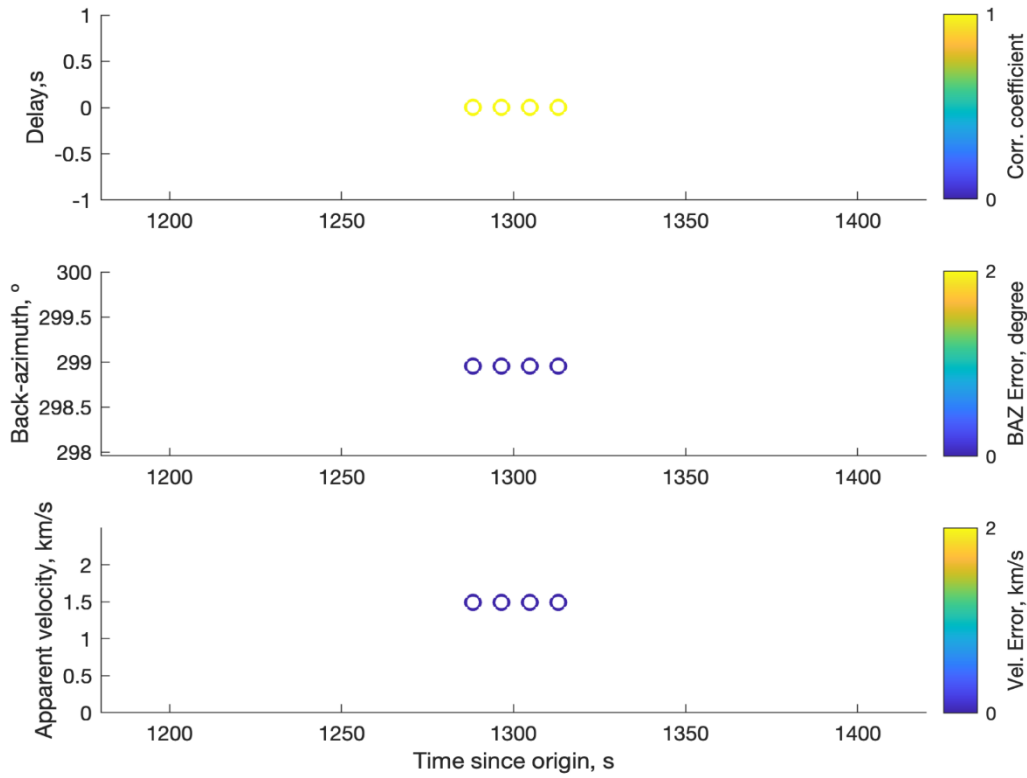
Figure S04. Results of the Mw 5.6 St. Paul earthquake occurred in 2023/01/03 at 18:19:29. Upper: Summed time delays obtained from lag times in cross-correlation and mean correlation coefficient between hydrophone pairs, showing a high correlation coefficient. Middle: Back-azimuths averaged from the three-hydrophone pair cross-correlated, with all the time windows showing the same back-azimuth. Bottom: Apparent sound velocity calculated as the mean across the array.
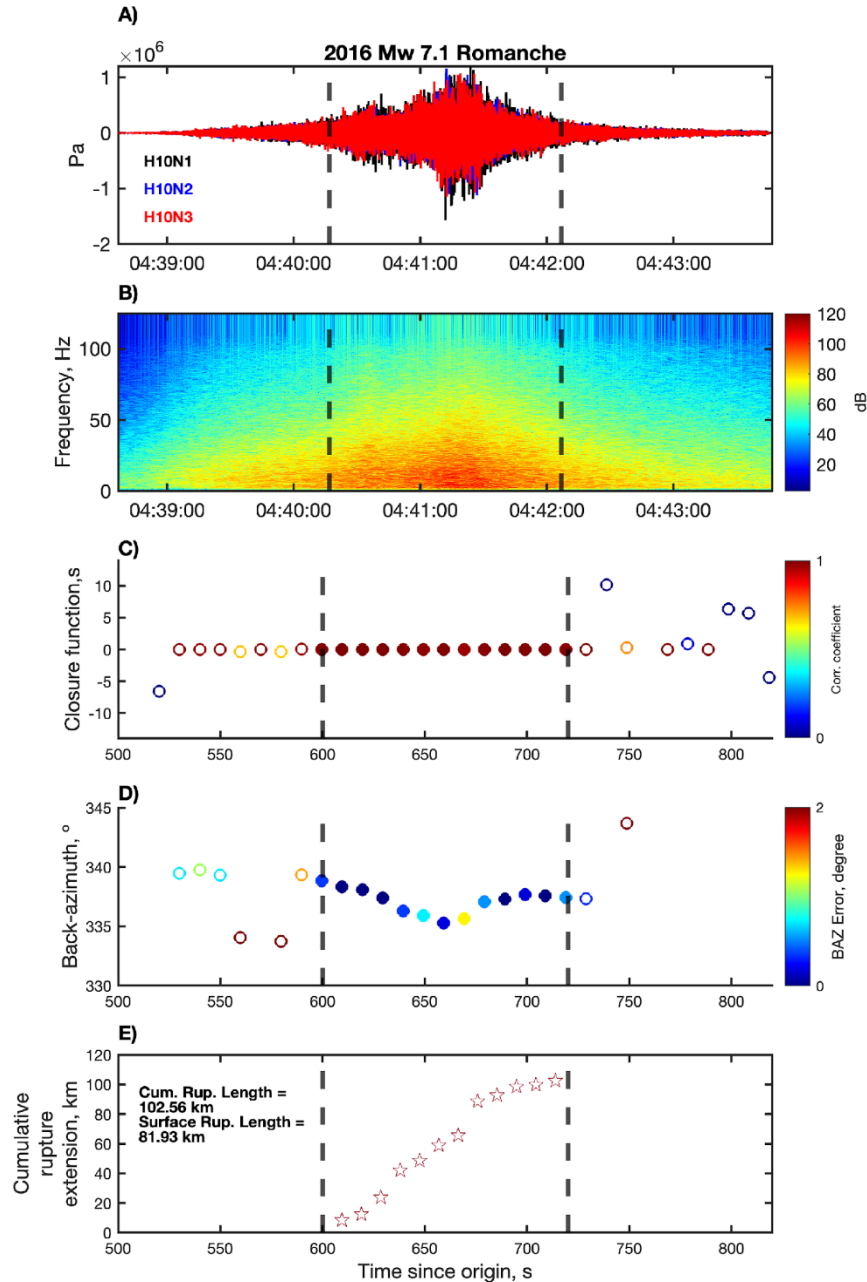
Figure S05. Hydroacoustic T-wave of the 2016 M_W 7.1 Romanche earthquake recorded at H10N hydrophone array. (a) shows the T waveforms of the three hydrophones superimposed with a 2 Hz high-pass filter to remove the lower frequency noise. Dotted lines indicate the start and end points of the analyzed waveform. They were selected from the higher energy observed from the single spectrogram of the H10N1 hydrophone shown in (b). The closure function of summed time delays obtained in cross-correlation between hydrophone pairs is shown in panel c). (d) back-azimuths averaged from the three-hydrophone pair cross-correlated. In (e), red stars indicate the cumulative distances for each time step adding up to the rupture length (RL).
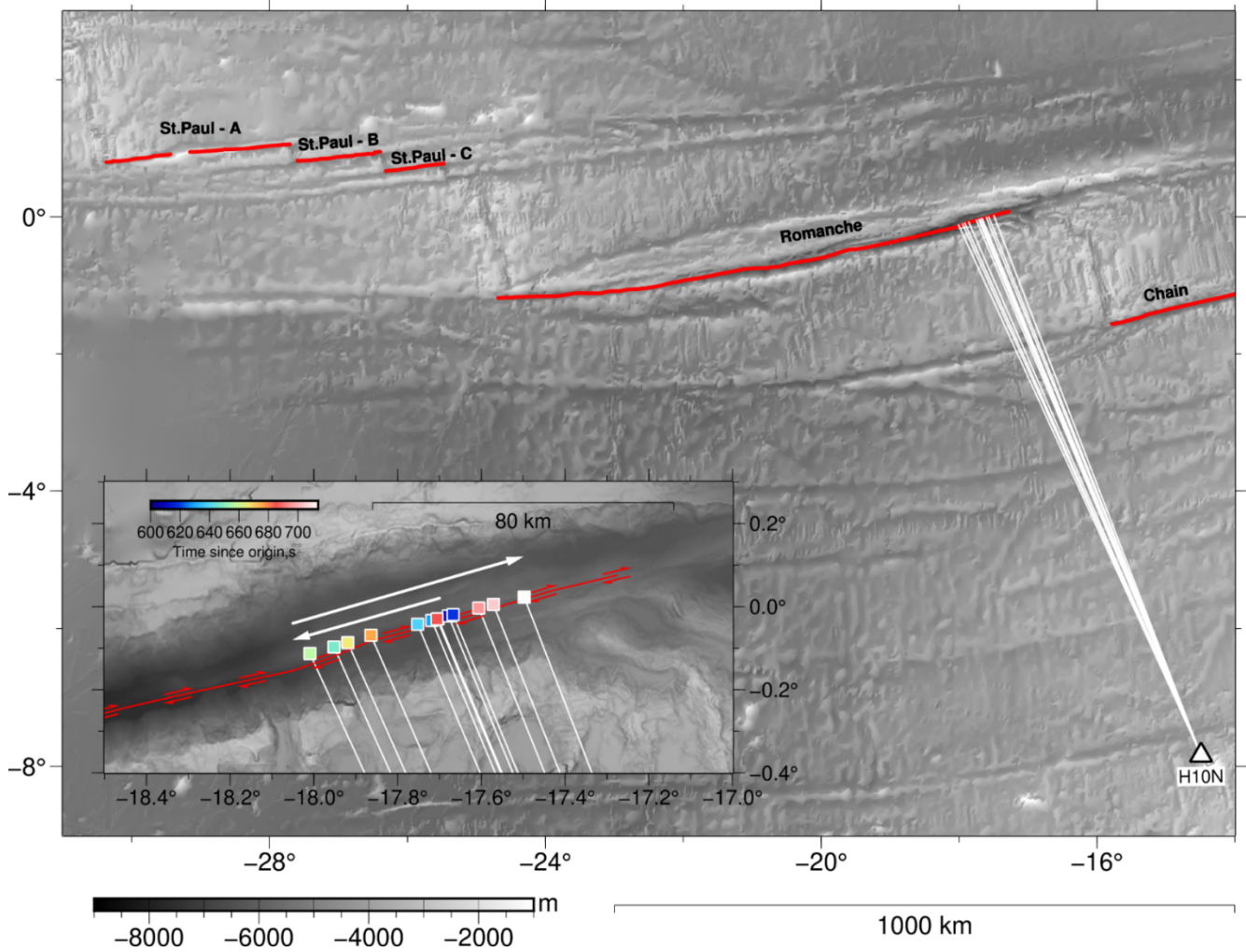
Figure S06. Bathymetric map of the equatorial Atlantic. White lines show the T-wave raypaths obtained from the back-azimuths analyzed with records in the H10N hydrophone array (white triangle) for the 2016 M_W 7.1 Romanche earthquake. Zoom-in of the rupture area is shown in the map on the left downside. Squares indicate the interception points of the ray paths over the mapped fault, with their color presenting the time of the propagation. The possible rupture directions are shown with the arrows.
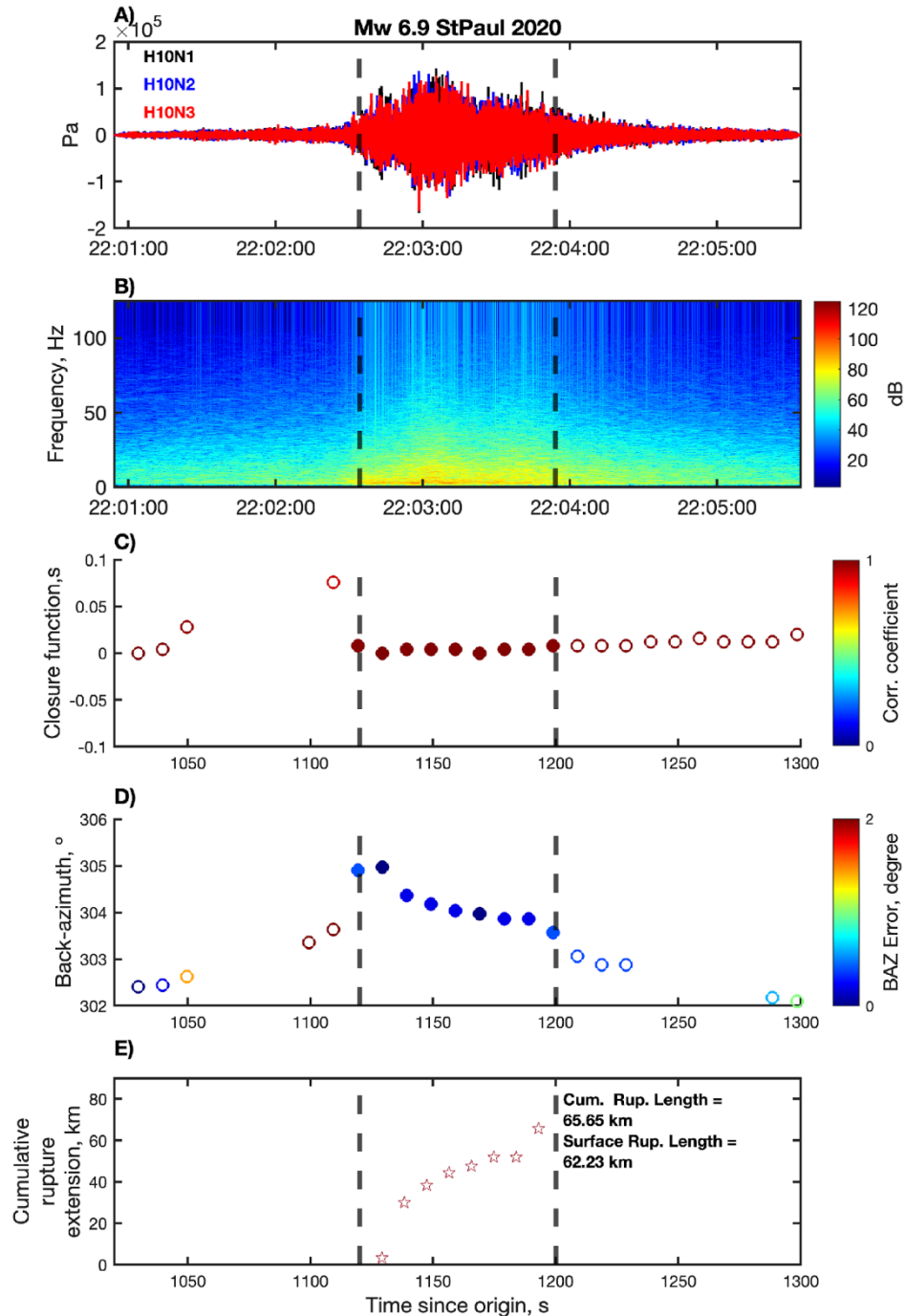
Figure S07. Hydroacoustic T-wave of the 2020 M_W 6.9 St. Paul earthquake recorded at H10N hydrophone array. (a) shows the T waveforms of the three hydrophones superimposed with a 2 Hz high-pass filter used to remove the lower frequency noise. Dotted lines present the start and end points of the analyzed waveform. They were selected from the higher energy observed from the single spectrogram of the H10N1 hydrophone shown in (b). The closure function of summed time delays obtained in cross-correlation between hydrophone pairs is shown in panel c). (d) back-azimuths averaged from the three-hydrophone pair cross-correlated. In (e), red stars indicate the cumulative distances for each time step, adding up to the rupture length (RL).
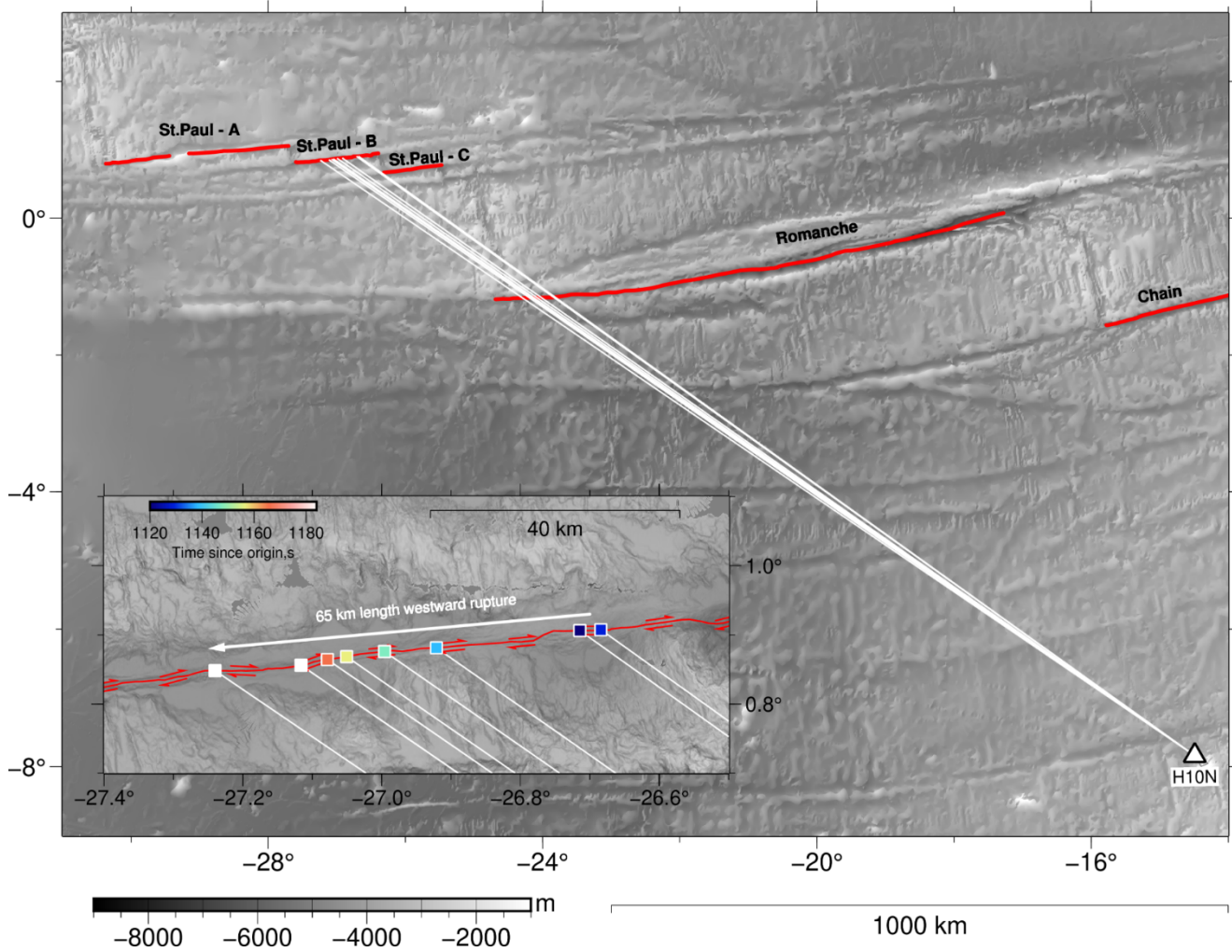
Figure S08. Bathymetric map of the equatorial Atlantic. White lines show the T-wave raypaths obtained from the back-azimuths analyzed with records in the H10N hydrophone array (white triangle) for the 2020 M_W 6.9 St. Paul earthquake. Zoom-in of the rupture area is shown in the map on the left downside. Squares indicate interception points of the ray paths with the mapped fault, with their color presenting the time of the propagation. The possible rupture direction is shown with the arrow.
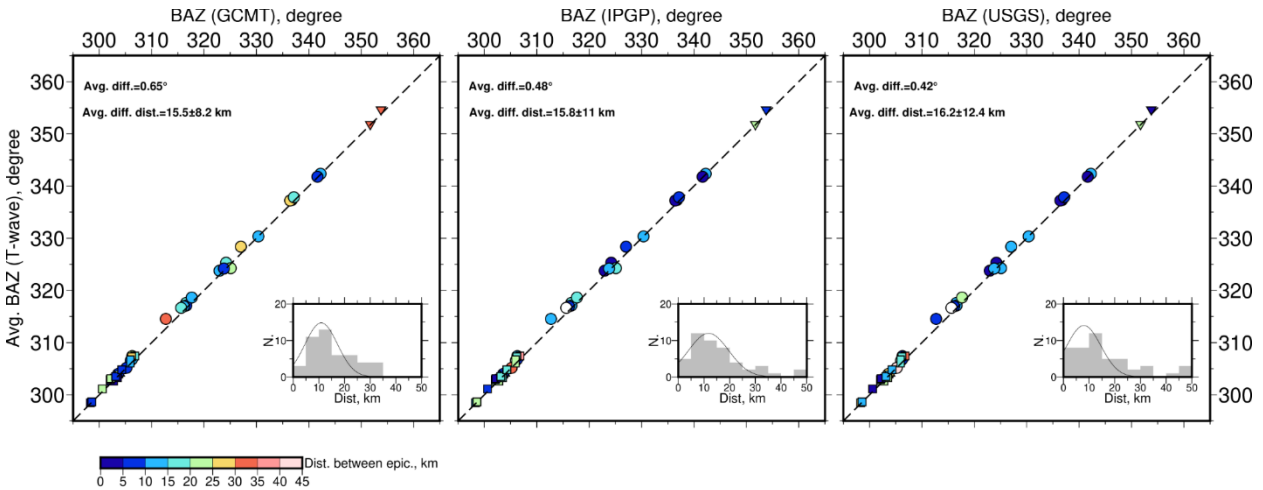
Figure S09. Comparison of the T-wave epicenter with global catalogs. Left/right plots show the comparison of back-azimuth between T-wave and GCMT/USGS epicenter locations. The middle plot refers to the comparison between T-wave and IPGP epicenter locations. The dotted lines indicate a slope of 1. Circles are colored by the distance between both epicenters.
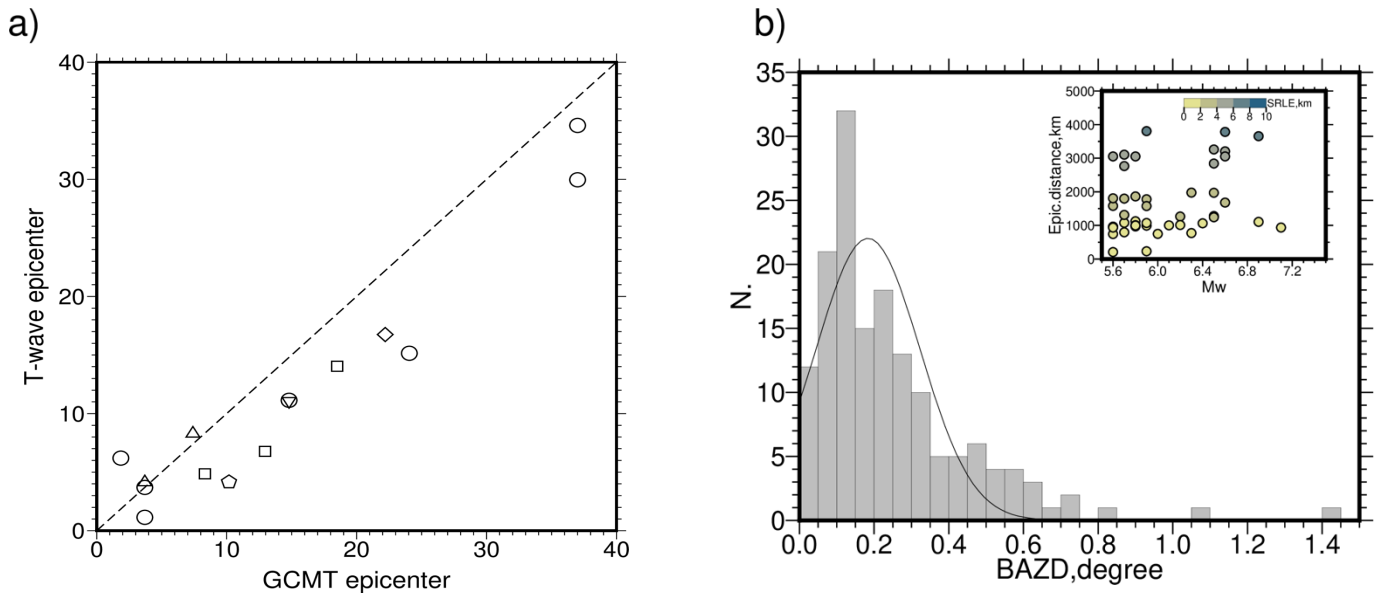
Figure S10. a) Comparison of the distance (km) between the relatively relocated earthquake pairs using the GCMT epicenter and their respective epicenters located using the T-wave. Circles refer to earthquakes of the Romanche transform. Three squares indicate earthquakes of the St. Paul A transform fault, with the single pentagon indicating the single earthquake identified along the St. Paul C transform. Earthquakes of the Vernadsky transform are shown with two triangles. The inverted triangle presents the Chain transform earthquake, and the single diamond symbol refers to an Ascension transform earthquake. b) Histogram showing the distribution of back-azimuth differences (BAZD) of all earthquakes. Independent of the epicentral distance, most BAZD are >0.1º, suggesting that angles $\geq 0.1°$ are well resolved.
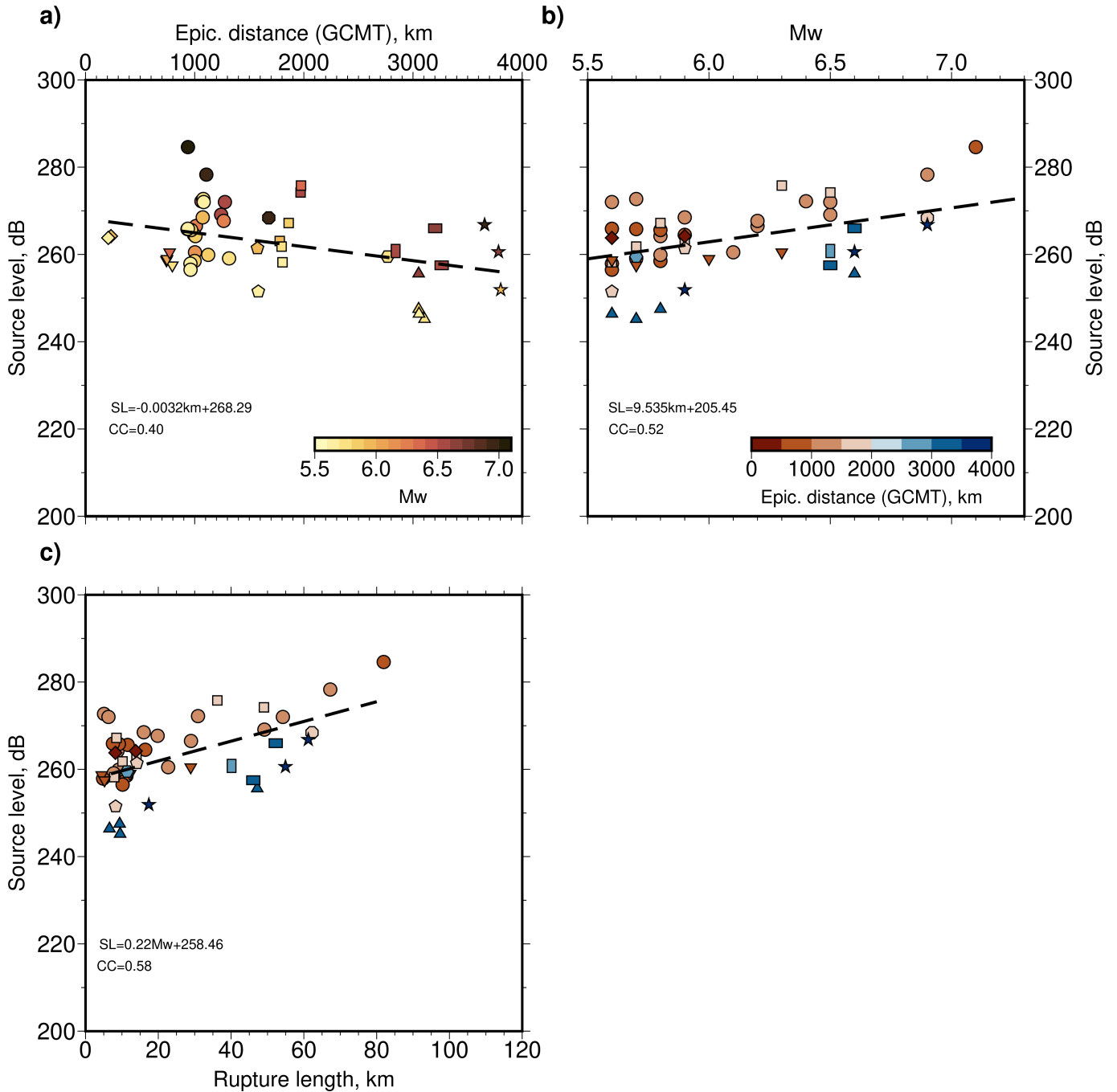
Figure S11. a) Effect of the source level (SL) compared to the epicentral distance. Color symbols show the moment magnitude of the respective earthquakes, suggesting a decrease of the SL with magnitudes. Symbols refer to oceanic transform faults (see Figure 2 in the main text). Dashed line shows the ordinary least square (OLS) regression fit of the comparison, with correlation coefficients of 0.40. b) Comparison between SL and the GCMT moment magnitude. Symbol color shows a gradual decrease of SL with increased epicentral distance (symbol colors). c) Comparison of source level versus rupture lengths in which a higher correlation coefficient of 0.58 was identified. The colors of symbols show that earthquakes with the same rupture lengths reveal a loss of the SL as the epicentral distance increases.
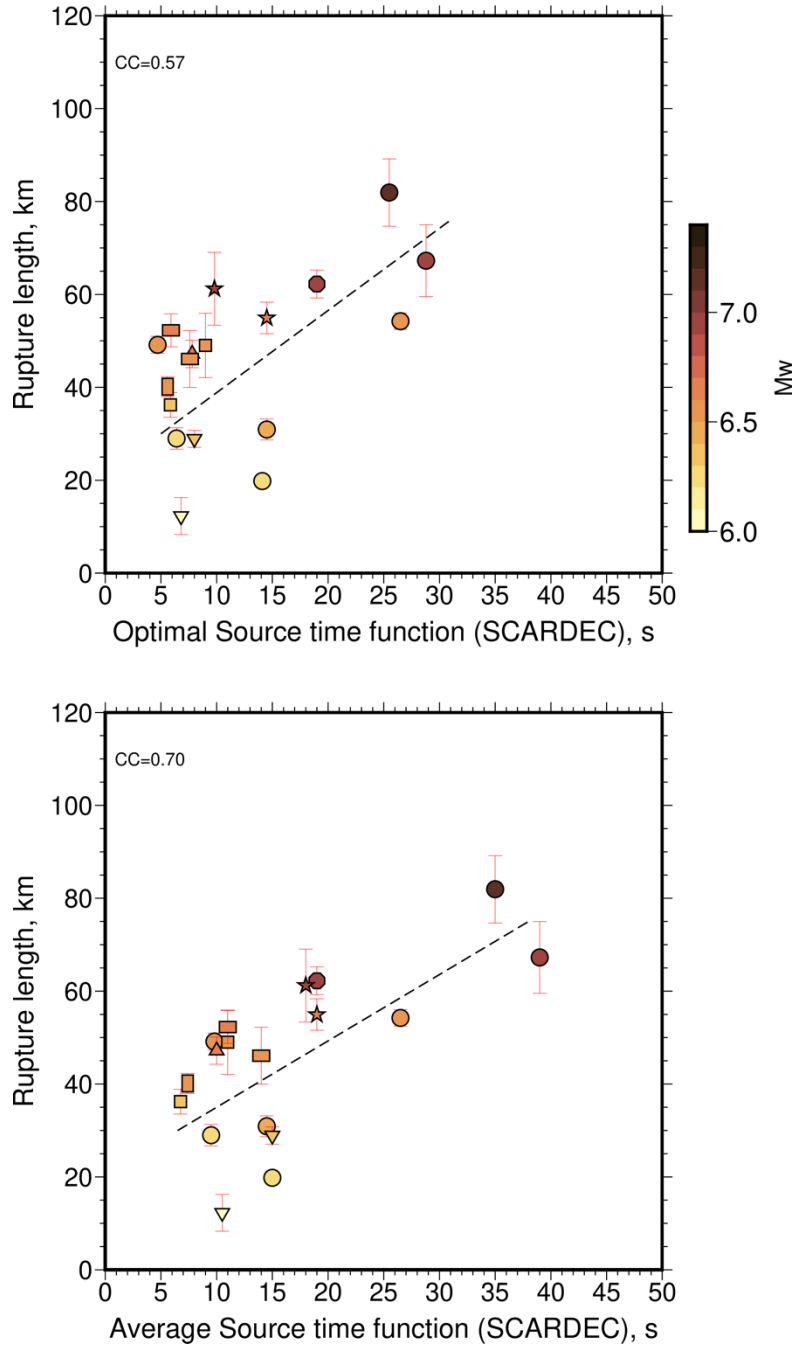
Figure S12. Rupture length versus source time function (SCARDEC). Upper panel: Comparison of the optimal source time function with rupture length. Circles refer to earthquakes that occurred in Romanche transform. Square/octagon refer to the St. Paul A and B transform, respectively. Earthquakes of the Vernadsky transform are shown in triangle symbols. Chain transform earthquakes are indicated with inverted triangles, and stars refer to the Vema transform. Vertical/horizontal rectangles show the earthquakes that occurred in Doldrums and Pushcharovsky transforms, respectively. The ordinary regression is shown by the dotted line, with a correlation coefficient of 0.57. Bottom: comparison with average source time function for the same earthquakes. The correlation showed a higher coefficient of 0.70.
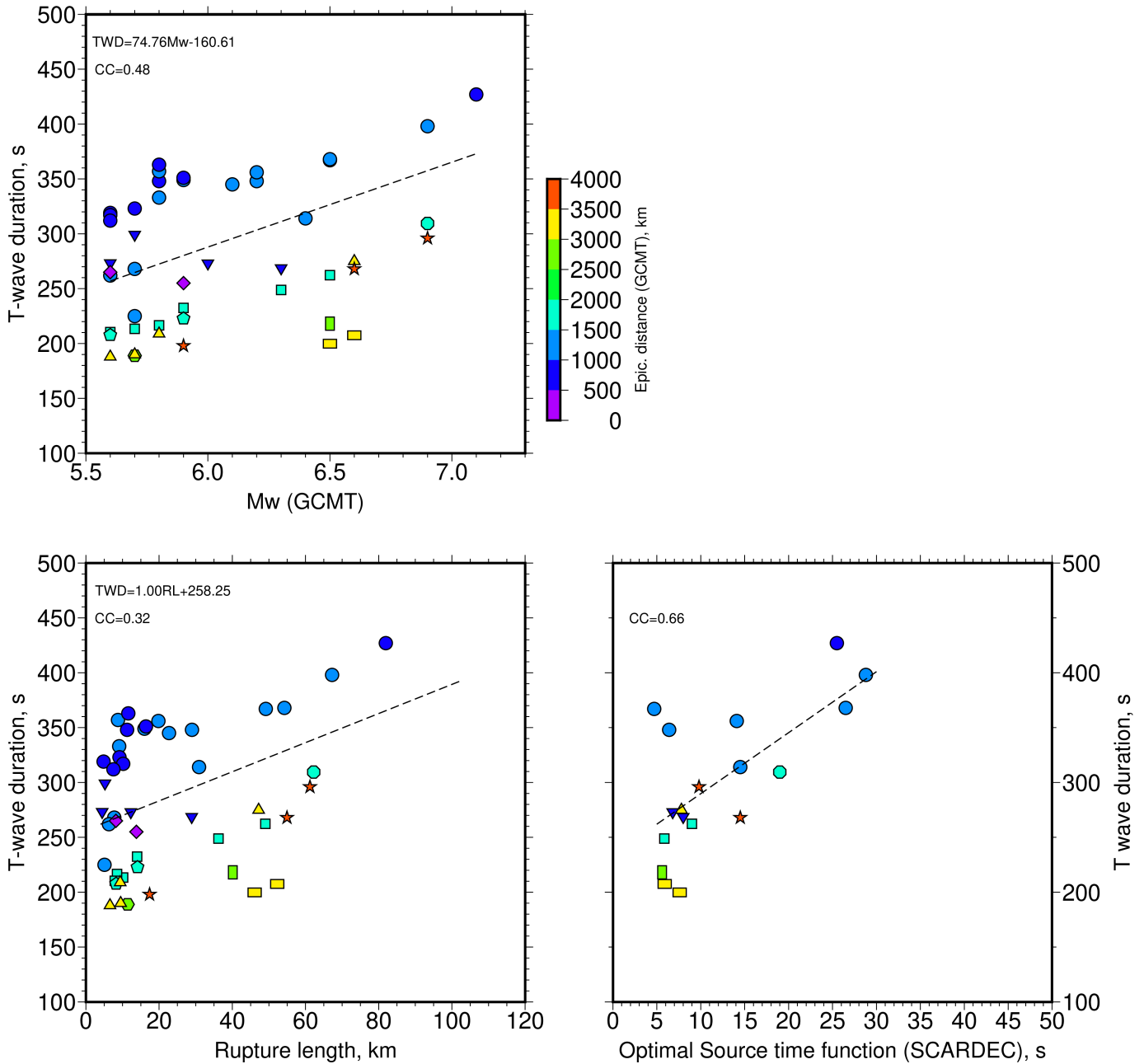
Figure S13. Comparisons of T-wave durations with global catalogues. Upper panel: Comparison of the total T-wave duration with Mw from GCMT. Circles refer to earthquakes that occurred in the Romanche transform. Symbols are the same as in Figure S14, besides the St. Paul C (pentagon), Bogdanov (hexagon), and Ascension (diamond) transform faults. Colors refer to the epicentral distance. The dotted line shows the least square regression. Bottom left: comparison of rupture length for the same respective events. Bottom right: Comparison of the T-wave duration with the optimal source time function (SCARDEC) for the respective earthquakes with the source time function available. The correlation showed a higher coefficient of 0.66.
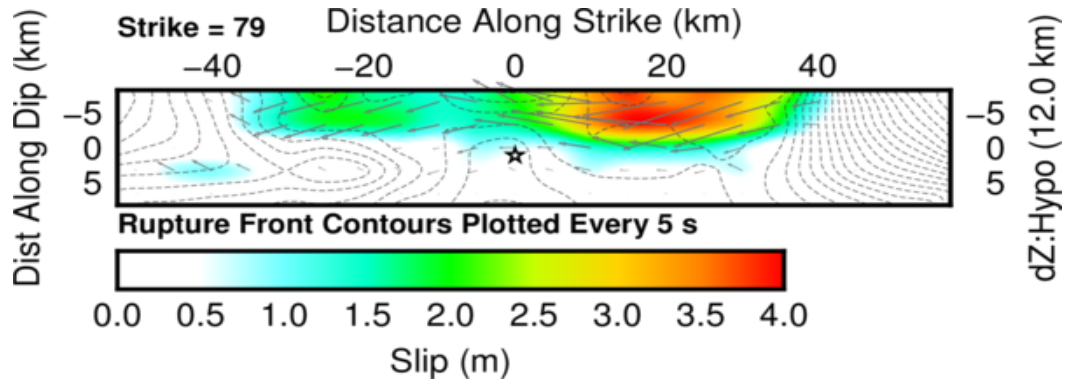
Figure S14. Cross-section of the slip distribution in strike direction of the 2016 Mw 7.1 Romanche earthquake (https://earthquake.usgs.gov/earthquakes/eventpage/us20006uy6/finite-fault). Star denotes the USGS hypocenter location.
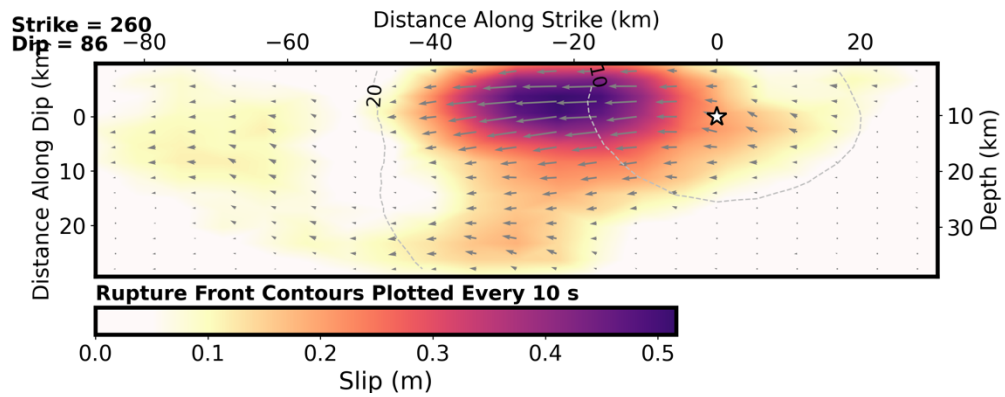
Figure S15. Cross-section of the slip distribution in strike direction of the 2020 Mw 6.9 Romanche earthquake (https://earthquake.usgs.gov/earthquakes/eventpage/us7000i53f/finite-fault). The USGS hypocenter location is denoted by a star.

Table S1. Rupture parameters of the 47 strike-slip earthquakes.

	Time	Lat °(GCMT)	Lon.(GCMT)	Mw(GCMT)	Cumulative rupture length, km	Cumulative rupture length error, km	RL, km	RLE, km	Rupture velocity, km/s	Rupture velocity error, km/s	Rupture type	Rupture direction
Ascension	22.08.20	-6.93	-12.59	5.9	13.79	0.61	13.79	0.40	0.83	0.29	Unilateral	Westward
	22.08.20	-6,96	-12.82	5.6	8.21	0.00	8.21	0.30	2.29	0.00	Unilateral	Eastward
Bogdanov	05.10.16	7.30	-34.33	5.7	11.42	1.42	11.41	4.82	1.25	0.34	Unilateral	Westward
Chain	27.10.16	-1.20	-15.44	5.6	4.50	0.28	4.44	1.30	0.20*	0.07	Unilateral	Eastward
	27.11.18	-0.71	-13.58	5.7	6.86	1.29	5.21	1.39	0.23*	0.16	Unilateral	Eastward
	10.03.18	-1.12	-15.12	6.0	14.67	3.97	12.27	1.30	0.99	0.80	Unilateral	Eastward
	23.10.19	-0.91	-13.72	6.3	38.69	1.86	28.90	1.34	1.21	0.41	Two-step	East-West
Doldrums	10.09.08	8.18	-38.54	6.6	63.33	3.54	52.28	5.59	1.91	0.77	Unilateral	Westward
	20.08.07	8.19	-39.17	6.5	46.09	6.12	46.09	5.69	2.79	1.48	Unilateral	Westward
Pushcharovsky	23.05.08	7.51	-35.01	6.5	43.40	2.16	40.14	4.95	1.08	0.47	Unilateral	Westward
Romanche	29.08.16	0.13	-17.72	7.1	102.56	7.25	81.93	1.63	2.70	0.59	Two-step	West-East
	04.09.22	-0.64	-21.23	6.9	89.10	7.72	67.25	1.93	2.44	2.39	Unilateral	Eastward
	30.11.17	-0.98	-23.35	6.5	53.40	1.83	49.14	2.16	1.46	0.40	Unilateral	Westward
	24.04.08	-1.14	-23.87	6.5	59.77	1.77	54.24	2.22	1.63	0.39	Unilateral	Westward
	09.12.09	-0.62	-20.80	6.4	33.18	2.25	30.91	1.85	2.02	0.96	Unilateral	Eastward
	08.02.22	-0.42	-19.81	6.2	21.78	2.31	19.82	2.20	2.56	1.09	Unilateral	Eastward
	09.10.22	-1.05	-23.52	6.2	32.63	1.24	28.99	1.76	1.02	0.27	Unilateral	Eastward
	17.08.23	-0.44	-19.78	6.1	25.38	1.17	22.70	1.74	1.54	0.28	Two-step	West-East

	29.12.20	-0.73	-21.08	5.9	15.99	4.53	15.99	1.87	4.76	1.01	Unilateral	Westward
	23.07.18	-0.18	-19.18	5.9	16.42	5.84	16.42	1.73	2.44	1.30	Unilateral	Westward
	18.08.23	-0.40	-19.61	5.8	11.24	0.10	11.24	1.74	4.57	0.01	Unilateral	Westward
	12.02.22	-0.49	-19.84	5.8	10.43	1.78	8.77	1.76	1.17	0.80	Unilateral	Westward
	24.09.20	-0.23	-18.80	5.8	11.57	5.78	11.57	1.69	2.58	2.58	Unilateral	Westward
	03.08.18	-0.69	-21.69	5.8	9.09	4.55	9.09	1.96	2.03	2.03	Unilateral	Westward
	01.09.21	-1.14	-24.28	5.7	7.75	0.40	7.75	2.29	3.46*	0.18	Unilateral	Westward
	22.03.20	-0.68	-21.09	5.7	6.45	1.86	5.09	1.88	1.44*	0.83	Unilateral	Eastward
	16.01.20	0.18	-17.12	5.7	9.16	0.73	9.16	1.63	2.25	0.33	Unilateral	Eastward
	23.07.15	-0.60	-21.05	5.6	7.51	3.28	7.51	1.68	2.13	1.39	Unilateral	Eastward
	24.11.15	0.18	-17.83	5.6	10.17	2.33	10.17	1.68	1.94	0.99	Unilateral	Eastward
	15.02.18	0.18	-17.84	5.6	7.05	0.30	4.83	1.68	1.57*	0.14	Unilateral	Eastward
	06.01.20	0.24	-17.05	5.6	6.31	0.66	6.30	1.64	2.11	0.30	Unilateral	Westward
St.Paul-A	30.08.20	0.84	-29.99	6.5	49.04	6.91	49.01	3.43	2.97	1.67	Unilateral	Westward
	03.07.07	0.81	-30.04	6.3	36.22	2.65	36.21	3.44	1.92	1.13	Unilateral	Westward
	05.08.19	1.13	-27.79	5.9	14.09	3.25	14.09	3.10	1.05	0.73	Unilateral	Westward
	27.01.16	1.13	-27.98	5.7	10.17	6.17	10.17	3.13	1.51	1.31	Unilateral	Eastward
	24.07.16	0.97	-28.77	5.8	13.46	7.90	8.52	3.25	2.74*	1.76	Unilateral	Eastward
	16.10.18	1.12	-28.07	5.6	7.90	2.18	7.90	3.15	3.35*	0.46	Unilateral	Westward
St.Paul-B	18.09.20	0.94	-26.91	6.9	65.65	3.00	62.23	2.92	1.80	0.66	Unilateral	Westward

St.Paul-C	11.09.23	0.85	-25.73	5.9	14.47	3.39	13.99	2.74	2.46	0.43	Unilateral	Westward
	06.10.17	0.92	-25.76	5.6	8.26	3.20	8.26	2.76	0.70*	0.41	Unilateral	Eastward
Vema	22.03.22	10.89	-43.06	6.6	61.24	3.39	54.95	6.60	3.73	1.45	Two-step	West-East
	30.10.20	10.92	-43.26	5.9	20.59	2.97	17.14	6.63	2.57	1.49	Unilateral	Eastward
	08.02.08	10.85	-41.71	6.9	73.00	7.85	61.22	6.38	2.07	0.65	Unilateral	Westward
Vernadsky	06.09.20	7.79	-37.18	6.6	50.29	2.95	47.20	5.32	1.57	0.65	Unilateral	Eastward
	23.03.19	7.79	-37.19	5.6	6.59	2.20	6.59	5.33	0.53*	0.53	Unilateral	Eastward
	07.10.18	7.80	-37.73	5.7	13.84	3.84	9.50	5.41	1.57*	0.93	Unilateral	Westward
	17.09.20	7.80	-37.14	5.8	9.35	3.12	9.35	5.32	0.76*	0.76	Unilateral	Eastward

*: rupture velocity might be difficult to resolve as maximum rupture length errors represent a substantial portion of the total surface rupture length.

Table S2. List of T-wave epicenters and the GCMT, IPGP, and USGS global catalogs.

	Date	New_Lat (°)	New_Long (°)	GCMT_Lat (°)	GCMT_Long (°)	IPGP_Lat(°)	IPGP_Long (°)	USGS_Lat(°)	USGS_Long(°)	BAZ_New (°)	BAZ_GCMT (°)	BAZ_IPGP (°)	BAZ_USGS (°)	Dist_to_GCMT (km)	Dist_to_IPGP (km)	Dist_to_USGS (km)
Ascension	22.08.20	-7.01	-12.72	-6.9600	-12.8200	-7.1	-12.94	-7.14	-12.97	65.18	62.17	64.45	65.09	12.78	26.73	30.82
Ascension	22.08.20	-6.96	-12.46	-6.9300	-12.5900	-7.10	-12.69	-7.19	-12.97	66.70	64.39	67.50	66.64	14.73	29.60	49.82
Bogdanov	05.10.16	7.17	-34.36	7.3000	-34.3300	7.13	-34.39	7.13	-34.44	306.47	306.94	306.53	306.45	14.84	5.28	9.92
Chain	27.10.16	-1.48	-15.41	-1.2000	-15.4400	-1.59	-15.59	-1.51	-15.59	351.72	351.84	349.98	350.12	31.00	23.84	20.66
Chain	27.11.18	-1.00	-13.58	-0.7100	-13.5800	-1.03	-13.66	-0.94	-13.73	7.65	7.29	6.94	6.32	32.50	9.59	17.78
Chain	10.03.18	-1.41	-15.18	-1.1200	-15.1200	-1.38	-15.25	-1.42	-15.21	353.78	354.63	353.31	353.58	32.50	7.59	3.46
Chain	23.10.19	-1.04	-13.70	-0.9100	-13.7200	-1.05	-13.83	-1.10	-13.84	6.71	6.36	5.60	5.54	1435	14.46	16.98
Doldrums	10.09.08	8.21	-39.18	8.1900	-39.1700	8.02	-39.27	8.04	-39.25	302.42	302.55	302.14	302.20	2.15	23.34	20.50
Doldrums	20.08.07	8.22	-38.55	8.1800	-38.5400	8.19	-38.70	8.09	-38.71	303.15	303.23	303.06	302.89	4.36	17.03	22.04

Pushcharovsky	23.05.08	7.39	-35.05	7.5100	-35.0100	7.26	-34.88	7.31	-34.90	305.94	306.39	306.10	306.17	13.78	23.85	19.51
Romanche	29.08.16	-0.76	-21.10	-0.6000	-21.0500	-0.63	-21.19	-0.69	-21.18	316.57	317.60	316.88	316.67	18.07	17.09	11.41
Romanche	04.09.22	-0.05	-17.80	0.1800	-17.8300	-0.13	-17.83	-0.10	-17.83	336.73	337.30	336.46	336.55	26.08	9.11	6.18
Romanche	30.11.17	-0.06	-17.85	0.1800	-17.8400	-0.07	-17.84	-0.07	-17.84	336.42	337.23	336.58	336.58	27.06	0.61	0.59
Romanche	24.04.08	0.13	-17.01	0.2400	-17.0500	0.23	-16.99	0.23	-16.99	342.24	342.35	342.74	342.74	12.42	11.16	11.14
Romanche	09.12.09	0.11	-17.10	0.1800	-17.1200	0.12	-17.09	0.12	-17.09	341.64	341.77	341.83	341.83	7.56	1.24	1.24
Romanche	08.02.22	-0.76	-21.09	-0.6800	-21.0900	-0.71	-21.18	-0.71	-21.18	316.60	317.11	316.63	316.63	8.39	11.23	11.25
Romanche	09.10.22	-1.14	-24.36	-1.1400	-24.2800	-1.11	-24.28	-1.24	-24.15	303.60	304.00	304.15	303.95	8.57	9.91	25.86
Romanche	17.08.23	-0.87	-21.92	-0.6900	-21.6900	-0.90	-22.03	-0.87	-22.00	312.71	314.55	312.34	312.61	32.51	12.56	7.97
Romanche	29.12.20	-0.29	-18.73	-0.2300	-18.8000	-0.28	-18.83	-0.24	-18.81	330.37	330.35	330.03	330.29	10.45	11.25	10.65
Romanche	23.07.18	-0.51	-19.95	-0.4900	-19.8400	-0.50	-19.99	-0.49	-19.99	322.94	323.78	322.99	323.04	12.51	4.35	4.58
Romanche	18.08.23	-0.47	-19.74	-0.4000	-19.6100	-0.45	-19.71	-0.45	-19.73	324.21	325.31	324.59	324.50	15.81	3.28	1.85
Romanche	12.02.22	-0.39	-19.26	-0.1800	-19.1800	-0.35	-19.23	-0.30	-19.25	327.03	328.38	327.51	327.58	25.31	5.70	10.56
Romanche	24.09.20	-0.77	-21.19	-0.7300	-21.0800	-0.76	-21.12	-0.76	-21.10	316.14	316.95	316.64	316.74	12.36	7.17	9.41
Romanche	03.08.18	-0.44	-19.59	-0.4400	-19.7800	-0.31	-19.57	-0.33	-19.58	325.09	324.27	325.85	325.72	21.42	15.05	12.42
Romanche	01.09.21	-0.48	-19.81	-0.4200	-19.8100	-0.40	-19.87	-0.42	-19.89	323.79	324.19	323.96	323.79	6.68	11.01	11.57
Romanche	22.03.20	-1.09	-23.59	-1.0500	-23.5200	-1.40	-23.88	-1.36	-23.90	306.03	306.59	304.08	304.15	8.53	47.10	46.62
Romanche	16.01.20	-0.73	-20.88	-0.6200	-20.8000	-0.73	-21.05	-0.69	-21.07	317.65	318.64	317.10	317.14	14.91	18.76	21.94
Romanche	23.07.15	-1.12	-23.83	-1.1400	-23.8700	-1.14	-23.56	-1.18	-23.47	305.19	305.17	306.12	306.20	5.32	30.24	40.23
Romanche	24.11.15	-1.08	-23.51	-0.9800	-23.3500	-1.11	-23.42	-1.08	-23.43	306.29	307.41	306.67	306.74	21.06	10.50	8.58
Romanche	15.02.18	-0.77	-21.29	-0.6400	-21.2300	-0.94	-21.72	-0.93	-21.72	315.63	316.66	313.42	313.45	15.20	47.00	48.57
Romanche	06.01.20	-0.04	-17.74	0.1300	-17.7200	-0.07	-17.81	-0.05	-17.83	337.14	337.85	336.74	336.73	18.94	8.82	9.43
St,Paul	30.08.20	0.75	-25.73	0.9200	-25.7600	0.98	-25.51	0.96	-25.51	306.78	307.44	308.28	308.20	19.33	35.55	33.48
St,Paul	03.07.07	1.01	-28.23	1.1200	-28.0700	0.95	-28.22	0.94	-28.22	302.08	302.90	302.10	302.08	21.35	6.53	7.30

St,Paul	05.08.19	1.02	-28.17	1.1300	-27.9800	0.98	-28.17	1.03	-28.15	302.20	303.11	302.30	302.47	24.75	3.62	3.08
St,Paul	27.01.16	0.96	-28.95	0.9700	-28.7700	0.93	-28.89	0.92	-28.97	300.58	301.12	300.78	300.60	20.27	7.09	4.89
St,Paul	24.07.16	1.05	-27.77	1.1300	-27.7900	1.03	-27.91	1.04	-27.87	303.14	303.50	302.95	303.07	8.75	16.62	11.58
St,Paul	16.10.18	0.71	-25.92	0.8500	-25.7300	0.75	-26.09	0.74	-26.09	306.17	307.29	306.08	306.03	25.69	19.45	19.67
St,Paul	18.09.20	0.83	-30.05	0.8100	-30.0400	0.74	-30.14	0.72	-30.27	298.30	298.47	298.12	297.83	2.19	13.60	27.42
St,Paul	11.09.23	0.85	-29.93	0.8400	-29.9900	0.87	-29.71	0.78	-29.87	298.57	298.64	299.19	298.67	7.00	24.92	10.28
St,Paul	06.10.17	0.88	-26.95	0.9400	-26.9100	0.96	-26.83	0.93	-26.85	304.29	304.79	305.03	304.89	8.13	15.87	12.25
Vena	22.03.22	10.83	-43.31	10.9200	-43.2600	10.62	-43.51	10.63	-43.53	302.50	302.84	302.16	302.16	11.81	31.58	32.02
Vema	30.10.20	10.82	-43.22	10.8900	-43.0600	10.81	-43.39	10.75	-43.38	302.59	302.98	302.55	302.46	18.76	19.09	19.94
Vema	08.02.08	10.77	-41.88	10.8500	-41.7100	10.71	-41.93	10.67	-41.90	303.79	304.22	303.79	303.76	20.32	8.93	11.09
Vernadsky	06.09.20	7.71	-37.19	7.7900	-37.1900	7.61	-37.12	7.53	-37.10	303.81	304.11	303.86	303.75	8.90	14.02	22.28
Vernadsky	23.03.19	7.71	-37.72	7.8000	-37.7300	7.66	-37.71	7.66	-37.71	303.18	303.48	303.26	303.27	9.60	5.98	6.04
Vernadsky	07.10.18	7.71	-37.16	7.8000	-37.1400	7.98	-37.01	7.78	-37.09	303.85	304.18	304.65	304.21	10.14	33.45	10.83
Vernadsky	17.09.20	7.71	-37.13	7.7900	-37.1800	7.70	-37.24	7.68	-37.15	303.89	304.12	303.89	303.96	10.46	12.22	4.24
													AVG	15.52	15.81	16.17
													STD	8.19	11.02	12.42

Table S3. Differences between surface waves and T-wave epicenter locations for the earthquake pairs analyzed.

Transform fault	Master event (YYYY, magnitude, date)	Relocated event (YYYY, magnitude, date)	Dist_rel_reloc. (km)	Dist_T_wave epics. (km)
Vernadsky	2020 Mw 6.6 - 06.09.20	2020 Mw 5.8 - 17.09.20	7.4	8.2953
Vernadsky	2020 Mw 6.6 - 06.09.20	2019 Mw 5.6 - 23.03.19	1.85	4.1444
StPaul_TransformC	2023 Mw 5.9 - 11.09.23	2017 Mw 5.6 - 06.10.17	10.175	4.1607
StPaul_TransformA	2020 Mw 6.5 - 30.08.20	2007 Mw 6.3 - 03.07.07	8.325	4.8593
StPaul_TransformA	2019 Mw 5.9 - 05.08.19	2016 Mw 5.7 - 27.01.16	18.5	14.0391

StPaul_TransformA	2018 Mw 5.6 - 16.10.18	2016 Mw 5.7 - 27.01.16	12.95	6.7727
Romanche	2023 Mw 6.1 - 17.08.23	2023 Mw 5.8 - 18.08.23	24.05	15.1452
Romanche	2022 Mw 6.9 - 04.09.22	2020 Mw 5.9 - 29.12.20	37	29.9543
Romanche	2022 Mw 6.2 - 09.10.22	2017 Mw 6.5 - 30.11.17	14.8	11.1359
Romanche	2020 Mw 5.8 - 24.09.20	2018 Mw 5.9 - 23.07.18	37	34.5926
Romanche	2020 Mw 5.7 - 16.01.20	2020 Mw 5.6 - 06.01.20	7.4	1.1454
Romanche	2020 Mw 5.7 - 22.03.20	2015 Mw 5.6 - 23.07.15	3.7	3.6981
Romanche	2018 Mw 5.6 - 15.02.18	2015 Mw 5.6 - 24.11.15	1.85	6.199
Chain	2019 Mw 6.3 - 23.10.19	2018 Mw 5.7 - 27.11.18	14.8	11.0677
Ascension	2020 Mw 5.9 - 22.08.20	2020 Mw 5.6 - 22.08.20	22.2	16.7463

Table S4. Hydroacoustic source levels and T-wave durations compared to the cumulative rupture lengths of the 47 strike-slip earthquakes.

	Date	Lat, ° (GCMT)	Long, ° (GCMT)	Mw (GCMT)	Cumulative rupture length, km	Receiver level (RL), dB	Total duration, s	Epicenter distance, km	Seafloor, m	Attenuation level (TL), dB	Final Source level, dB
Ascension	22.08.20	-6.93	-12.59	5.9	13.79	175.0	255.0	232.5	-3521.64	89.13	264.2
	22.08.20	-6.96	-12.82	5.6	8.21	175.5	265.0	208.4	-3242.28	88.30	263.8
Bogdanov	05.10.16	7.30	-34.33	5.7	11.42	160.9	188.9	2766.2	-2590.60	98.55	259.5
Chain	27.10.16	-1.20	-15.44	5.6	4.50	165.3	273.0	741.6	-2961.66	93.42	258.7
	27.11.18	-0.71	-13.58	5.7	6.86	162.9	299.0	794.7	-3618.91	94.59	257.5
	10.03.18	-1.12	-15.12	6.0	14.67	165.2	273.0	746.2	-3249.38	93.85	259.0
	23.10.19	-0.91	-13.72	6.3	38.69	165.2	268.0	770.9	-4327.75	95.23	260.5
Doldrums	10.09.08	8.18	-38.54	6.6	63.33	164.8	207.0	3202.9	-4128.23	101.21	266.0
	20.08.07	8.19	-39.17	6.5	46.09	156.4	199.0	3261.9	-4010.24	101.17	257.5
Pushcharovsky	23.05.08	7.51	-35.01	6.5	43.40	160.3	218.0	2840.3	-3968.32	100.52	260.8
Romanche	29.08.16	0.13	-17.72	7.1	102.56	188.2	427.0	937.9	-4663.42	96.41	284.6
	04.09.22	-0.64	-21.23	6.9	89.10	181.7	398.0	1107.0	-4098.43	96.57	278.3

	30.11.17	-0.98	-23.35	6.5	53.40	172.1	378.0	1241.9	-4097.90	97.07	269.1
	24.04.08	-1.14	-23.87	6.5	59.77	173.6	368.0	1277.1	-5385.20	98.37	272.0
	09.12.09	-0.62	-20.80	6.4	33.18	174.8	314.0	1061.7	-5172.24	97.40	272.2
	08.02.22	-0.42	-19.81	6.2	21.78	169.2	358.0	1010.6	-5298.36	97.29	266.5
	09.10.22	-1.05	-23.52	6.2	32.63	169.8	362.0	1266.0	-4866.90	97.90	267.7
	17.08.23	-0.44	-19.78	6.1	25.38	163.4	345.0	1002.4	-5114.09	97.10	260.5
	29.12.20	-0.73	-21.08	5.9	15.99	170.2	349.0	1073.5	-6271.90	98.28	268.5
	23.07.18	-0.18	-19.18	5.9	16.42	168.3	351.0	994.0	-4238.23	96.25	264.5
	18.08.23	-0.40	-19.61	5.8	11.24	161.8	348.0	998.7	-4651.61	96.67	258.5
	12.02.22	-0.49	-19.84	5.8	10.43	167.0	357.0	1006.3	-5205.53	97.19	264.2
	24.09.20	-0.23	-18.80	5.8	11.57	168.9	363.0	967.8	-4918.96	96.78	265.6
	03.08.18	-0.69	-21.69	5.8	9.09	163.2	333.0	1123.8	-4121.31	96.66	259.9
	01.09.21	-1.14	-24.28	5.7	7.75	161.0	268.0	1314.5	-4968.12	98.15	259.1
	22.03.20	-0.68	-21.09	5.7	6.45	175.1	225.0	1078.3	-5336.54	97.60	272.7
	16.01.20	0.18	-17.12	5.7	9.16	168.2	323.0	933.5	-6270.57	97.67	265.8
	23.07.15	-0,60	-21.05	5.6	7.51	175.5	262.0	1081.8	-4183.84	96.56	272.0
	24.11.15	0.18	-17.83	5.6	10.17	164.4	319.0	961.0	-2307.45	93.46	257.9
	15.02.18	0.18	-17.84	5.6	7.05	163.3	317.0	961.5	-2198.46	93.25	256.5
	06.01.20	0.24	-17.05	5.6	6.31	169.4	312.0	937.4	-4838.71	96.57	265.9
St.Paul-A	30.08.20	0.84	-29.99	6.5	49.04	176.1	262.3	1970.1	-3293.66	98.12	274.2
	03.07.07	0.81	-30.04	6.3	36.22	177.7	248.8	1973.4	-3276.24	98.11	275.8
	05.08.19	1.13	-27.79	5.9	14.09	166.2	232.4	1778.7	-2748.85	96.89	263.1
	27.01.16	1.13	-27.98	5.7	10.17	163.9	213.4	1796.2	-3403.20	97.86	261.8
	24.07.16	0.97	-28.77	5.8	13.46	170.5	216.6	1860.6	-2543.37	96.75	267.2
	16.10.18	1.12	-28.07	5.6	7.90	160.4	210.4	1803.9	-3401.49	97.88	258.2
St.Paul-B	18.09.20	0.94	-26.91	6.9	65.65	174.4	309.5	678.4	-3676.98	93.97	268.4
St.Paul-C	11.09.23	0.85	-25.73	5.9	14.47	164.2	222.7	1574.8	-3298.50	97.16	261.4
	06.10.17	0.92	-25.76	5.6	8.26	154.8	207.7	1582.1	-2951.75	96.69	251.5
Vema	22.03.22	10.89	-43.06	6.6	61.24	157.7	268.0	3782.5	-5142.31	102.89	260.6
	30.10.20	10.92	-43.26	5.9	20.59	149.6	198.0	3803.2	-4455.30	102.29	251.9
	08.02.08	10.85	-41.71	6.9	73.00	164.2	296.0	3655.8	-5004.61	102.62	266.8
Vernadsky	06.09.20	7.79	-37.18	6.6	50.29	155.6	275.0	3051.5	-3264.11	99.98	255.6
	23.03.19	7.79	-37.19	5.6	6.59	146.2	188.0	3055.0	-3438.26	100.21	246.4

	07.10.18	7.80	-37.73	5.7	13.84	147.2	190.0	3105.2	-2061.75	98.06	245.2
	17.09.20	7.80	-37.14	5.8	9.35	147.8	209.0	3051.5	-3055.69	99.70	247.5

References

Bickert, M., Kaczmarek, M. A., Brunelli, D., Maia, M., Campos, T. F., & Sichel, S. E. (2023). Fluid-assisted grain size reduction leads to strain localization in oceanic transform faults. *Nature Communications*, *14*(1), 4087. https://doi.org/10.1038/s41467-023-39556-5

Blackman, D. K., Karson, J. A., Kelley, D. S., Cann, J. R., Früh-Green, G. L., Gee, J. S., ... & Williams, E. A. (2002). Geology of the Atlantis Massif (Mid-Atlantic Ridge, 30 N): Implications for the evolution of an ultramafic oceanic core complex. *Marine Geophysical Researches*, *23*, 443-469. https://doi.org/10.1023/B:MARI.0000018232.14085.75

Bohnenstiehl, D. R., Tolstoy, M., Smith, D. K., Fox, C. G., & Dziak, R. P. (2003). Time-clustering behavior of spreading-center seismicity between 15 and 35 N on the Mid-Atlantic Ridge: Observations from hydroacoustic monitoring. *Physics of the Earth and Planetary Interiors*, *138*(2), 147-161. https://doi.org/10.1016/S0031-9201(03)00113-4

Buehler, J. S., & Shearer, P. M. (2014). Anisotropy and Vp/Vs in the uppermost mantle beneath the western United States from joint analysis of Pn and Sn phases. *Journal of Geophysical Research: Solid Earth*, *119*(2), 1200-1219. https://doi.org/10.1002/2013JB010559

Campos, T. F. C., Neto, J. V., Amorim, V. A., Hartmann, L. A., & Petta, R. A. (2003). Modificações metassomáticas das rochas milonitizadas do complexo ultramáfico do Arquipélago de São Pedro e São Paulo, Atlântico Equatorial. *Geochimica Brasiliensis*, *17*(2). https://geobrasiliensis.org.br/geobrasiliensis/article/view/201

Campos, T. F., Sichel, S. E., Maia, M., Brunelli, D., Motoki, K., Magini, C., ... & de Melo, G. (2022). The singular St. Peter and St. Paul Archipelago, equatorial Atlantic, Brazil. In *Meso-Cenozoic Brazilian Offshore Magmatism* (pp. 121-165). Academic Press. https://doi.org/10.1016/B978-0-12-823988-9.00003-4

Christensen, N. I. (1996). Poisson's ratio and crustal seismology. *Journal of Geophysical Research: Solid Earth*, *101*(B2), 3139-3156. https://doi.org/10.1029/95JB03446

de Groot-Hedlin, C. D. (2005), Estimation of the rupture length and velocity of the great sumatra earthquake of dec 26, 2004 using hydroacoustic signals, *Geophysical Research Letters, 32* (11). https://doi.org/10.1029/2005GL022695

Dziak, R. P. (2001). Empirical relationship of T-wave energy and fault parameters of northeast Pacific Ocean earthquakes. *Geophysical Research Letters*, *28*(13), 2537-2540. https://doi.org/10.1029/2001GL012939

Erbe, C. (2011). Underwater acoustics: noise and the effects on marine mammals. *A Pocket Handbook*, 3rd edition, JASCO Applied Science, 23p.

Ekström, G., Nettles, M., & Dziewoński, A. M. (2012). The global CMT project 2004–2010: Centroid-moment tensors for 13,017 earthquakes. *Physics of the Earth and Planetary Interiors*, *200*, 1-9. https://doi.org/10.1016/j.pepi.2012.04.002

Guilbert, J., Vergoz, E. Chissele, A. Roueff, & Y. Cansi (2005), Use of hydroacoustic and seismic arrays to observe rupture propagation and source extent of the mw= 9.0 sumatra earthquake, Geophysical Research Letters, 32 (15). https://doi.org/10.1029/2005GL022966

Gregory, E. P., Singh, S. C., Marjanović, M., & Wang, Z. (2021). Serpentinized peridotite versus thick mafic crust at the Romanche oceanic transform fault. *Geology*, *49*(9), 1132-1136. https://doi.org/10.1130/G49097.1

Grevemeyer, I., Reston, T. J., & Moeller, S. (2013). Microseismicity of the Mid-Atlantic Ridge at 7° S–8° 15′ S and at the Logatchev Massif oceanic core complex at 14° 40′ N–14° 50′ N. *Geochemistry, Geophysics, Geosystems*, *14*(9), 3532-3554. https://doi.org/10.1002/ggge.20197

Grevemeyer, I., Hayman, N. W., Peirce, C., Schwardt, M., Van Avendonk, H. J., Dannowski, A., & Papenberg, C. (2018). Episodic magmatism and serpentinized mantle exhumation at an ultraslow-spreading centre. *Nature Geoscience*, *11*(6), 444-448. https://doi.org/10.1038/s41561-018-0124-6

Hekinian, R., Juteau, T., Gracia, E., Sichler, B., Sichel, S., Udintsev, G., ... & Ligi, M. (2000). Submersible observations of equatorial atlantic mantle: the St. Paul Fracture Zone region. *Marine Geophysical Researches*, *21*, 529-560. https://doi.org/10.1023/A:1004819701870

Ji, C., Wald, D. J., & Helmberger, D. V. (2002). Source description of the 1999 Hector Mine, California, earthquake, part I: Wavelet domain inversion theory and resolution analysis. *Bulletin of the Seismological Society of America*, *92*(4), 1192-1207. https://doi.org/10.1785/0120000916

Ji, S., Li, A., Wang, Q., Long, C., Wang, H., Marcotte, D., & Salisbury, M. (2013). Seismic velocities, anisotropy, and shear-wave splitting of antigorite serpentinites and tectonic implications for subduction zones. *Journal of Geophysical Research: Solid Earth*, *118*(3), 1015-1037. https://doi.org/10.1002/jgrb.50110

Kanamori, H. (1977). The energy release in great earthquakes. *Journal of Geophysical Research*, *82*(20), 2981-2987. https://doi.org/10.1029/JB082i020p02981

Metz, D., Nielson, P., Zampolli, M., Haralabus, G. (2021). Remote detection of hydroacoustic signals potentially associated with the sinking of SS El Faro using CTBT IMS hydrophone data. In CTBT Science and Technology Conference (Vol. 2021, pp. P1.3-331).

Li, Z., Wiens, D. A., Shen, W., & Shillington, D. J. (2024). Along-strike variations of Alaska subduction zone structure and hydration determined from amphibious seismic data. *Journal of Geophysical Research: Solid Earth*, *129*(3), e2023JB027800. https://doi.org/10.1029/2023JB027800

Liu, T., Gong, J., Fan, W., & Lin, G. (2023). In-situ Vp/Vs reveals fault-zone material variation at the westernmost Gofar Transform Fault, East Pacific Rise. *Journal of Geophysical Research: Solid Earth*, *128*(3), e2022JB025310. https://doi.org/10.1029/2022JB025310

McGuire, J. J. (2008). Seismic cycles and earthquake predictability on East Pacific Rise transform faults. *Bulletin of the Seismological Society of America*, *98*(3), 1067-1084. https://doi.org/10.1785/0120070154

Okal, E. A. (2008). The generation of T waves by earthquakes. *Advances in geophysics*, *49*, 1-65. https://doi.org/10.1016/j.pepi.2009.03.002

Pan, J., Antolik, M., & Dziewonski, A. M. (2002). Locations of mid-oceanic earthquakes constrained by seafloor bathymetry. *Journal of Geophysical Research: Solid Earth*, *107*(B11), EPM-8. https://doi.org/10.1029/2001JB001588

Pan, J., & Dziewonski, A. M. (2005). Comparison of mid-oceanic earthquake epicentral differences of travel time, centroid locations, and those determined by autonomous underwater hydrophone arrays. *Journal of Geophysical Research: Solid Earth*, *110*(B7). https://doi.org/10.1029/2003JB002785

Parsons, B., & Sclater, J. G. (1977). An analysis of the variation of ocean floor bathymetry and heat flow with age. *Journal of Geophysical Research*, *82*(5), 803-827. https://doi.org/10.1029/JB082i005p00803

Romanowicz, B., Cara, M., Fel, J. F., & Rouland, D. (1984). GEOSCOPE: A French initiative in long-period three-component global seismic networks. *Eos, Transactions American Geophysical Union*, *65*(42), 753-753. https://doi.org/10.1029/EO065i042p00753-01

Shearer, P., & Bürgmann, R. (2010). Lessons learned from the 2004 Sumatra-Andaman megathrust rupture. *Annual Review of Earth and Planetary Sciences*, *38*(1), 103-131. https://doi.org/10.1146/annurev-earth-040809-152537

Searle, R. (2013). *Mid-ocean ridges*. Cambridge University Press. https://doi.org/10.1017/CBO9781139084260

Seton, M., Müller, R. D., Zahirovic, S., Williams, S., Wright, N. M., Cannon, J., ... & McGirr, R. (2020). A global data set of present-day oceanic crustal age and seafloor spreading parameters. *Geochemistry, Geophysics, Geosystems*, *21*(10), e2020GC009214. https://doi.org/10.1029/2020GC009214

Scholz, C. (1988), The brittle-plastic transition and the depth of seismic faulting, *Geologische Rundschau*, *77*, 319–328. https://doi.org/10.1007/BF01848693

Talandier, J., & Okal, E. A. (1998). On the mechanism of conversion of seismic waves to and from T waves in the vicinity of island shores. *Bulletin of the Seismological Society of America*, *88*(2), 621-632. https://doi.org/10.1785/BSSA0880020621

Toda, S., Stein, R. S., Sevilgen, V., & Lin, J. (2011). Coulomb 3.3 Graphic-rich deformation and stress-change software for earthquake, tectonic, and volcano research and teaching—user guide. *US Geological Survey open-file report*, *1060*(2011), 63. https://pubs.usgs.gov/of/2011/1060/

Tolstoy, M., & D. R. Bohnenstiehl (2005), Hydroacoustic constraints on the rupture duration, length, and speed of the great sumatra-andaman earthquake, *Seismological Research Letters, 76* (4), 419–425. https://doi.org/10.1785/gssrl.76.4.419

Tozer, B., Sandwell, D. T., Smith, W. H., Olson, C., Beale, J. R., & Wessel, P. (2019). Global bathymetry and topography at 15 arc sec: SRTM15+. *Earth and Space Science*, *6*(10), 1847-1864.

Turcotte, D. L., & Schubert, G. (2002). *Geodynamics*. Cambridge University Press. https://doi.org/10.1017/CBO9780511843877

U.S. Geological Survey, 2024, Earthquake Lists, Maps, and Statistics, accessed April, 2024 at URL https://earthquake.usgs.gov/earthquakes/search/

Vallée, M., & Douet, V. (2016). A new database of source time functions (STFs) extracted from the SCARDEC method. *Physics of the Earth and Planetary Interiors*, *257*, 149-157. https://doi.org/10.1016/j.pepi.2016.05.012

Wang, Z., Singh, S. C., Prigent, C., Gregory, E. P., & Marjanović, M. (2022). Deep hydration and lithospheric thinning at oceanic transform plate boundaries. *Nature Geoscience*, *15*(9), 741-746. https://doi.org/10.1038/s41561-022-01003-3